Physics of Plasmas

Magnetized laser–plasma interactions in high-energy-density systems: Parallel propagation

Cite as: Phys. Plasmas **29**, 042113 (2022); https://doi.org/10.1063/5.0079547
Submitted: 22 November 2021 • Accepted: 25 March 2022 • Published Online: 13 April 2022

E. E. Los and D. J. Strozzi

Physics of Plasmas ARTICLE scitation.org/journal/php

Magnetized laser–plasma interactions in high-energy-density systems: Parallel propagation

Cite as: Phys. Plasmas **29**, 042113 (2022); doi: 10.1063/5.0079547
Submitted: 22 November 2021 · Accepted: 25 March 2022 ·
Published Online: 13 April 2022

View Online Export Citation CrossMark

E. E. Los[1,a)] and D. J. Strozzi[2]

AFFILIATIONS

[1]Physics Department, Imperial College London, South Kensington Campus, London SW7 2AZ, United Kingdom
[2]Lawrence Livermore National Laboratory, Livermore, California 94551, USA

[a)]Author to whom correspondence should be addressed: e.los18@imperial.ac.uk

ABSTRACT

We investigate parametric processes in magnetized plasmas, driven by a large-amplitude pump light wave. Our focus is on laser–plasma interactions relevant to high-energy-density (HED) systems, such as the National Ignition Facility and the Sandia MagLIF concept. We present a self-contained derivation of a "parametric" dispersion relation for magnetized three-wave interactions, meaning the pump wave is included in the equilibrium, similar to the unmagnetized work of Drake *et al.*, Phys. Fluids **17**, 778 (1974). For this, we use a multi-species plasma fluid model and Maxwell's equations. The application of an external B field causes right- and left-polarized light waves to propagate with differing phase velocities. This leads to Faraday rotation of the polarization, which can be significant in HED conditions. Phase-matching and linear wave dispersion relations show that Raman and Brillouin scattering have modified spectra due to the background B field, though this effect is usually small in systems of current practical interest. We study a scattering process we call stimulated whistler scattering, where a light wave decays to an electromagnetic whistler wave ($\omega \lesssim \omega_{ce}$) and a Langmuir wave. This only occurs in the presence of an external B field, which is required for the whistler wave to exist.

I. INTRODUCTION

Imposing a magnetic field on high-energy-density (HED) systems is a topic of much current interest. This has several motivations, including reduced electron thermal conduction to create hotter systems (such as for x-ray sources[1]), laboratory astrophysics,[2] and magnetized inertial confinement fusion (ICF) schemes. If successful, they could provide efficient, low-cost alternatives to unmagnetized, laser-driven ICF. In the most successful case, the Sandia MagLIF concept,[3,4] an external axial magnetic field, is used to magnetize the deuterium–tritium (DT) gas contained within a cylindrical conducting liner. A pulsed-power machine then discharges a high current through the liner, generating a Lorentz force which causes the liner to implode. The DT fuel is pre-heated by a laser as the implosion alone is not sufficient to heat the fuel to the ignition temperature. The magnetic field is confined within the liner and in the absence of diffusion or other flux loss obeys flux conservation, which states

$$B_z \pi r^2 = c, \tag{1}$$

where r is the radius of the cylindrical liner, B_z is the axial magnetic field, and c is a constant. Over the course of the implosion, the magnetic field strength perpendicular to the direction of compression increases as $1/r^2$. Thus, following the implosion, the magnetic field traps fusion alpha particles and thermal electrons, insulating the target and aiding ignition.

The MagLIF scheme, as well as magnetized laser-driven ICF,[5,6] and magnetized parametric laser amplification[7] motivate us to consider magnetized laser–plasma interactions (LPI), specifically parametric scattering processes.[8] The parametric coupling involves the decay of a large-amplitude or "pump" wave into two or more daughter waves. We focus on the decay of an electromagnetic (e/m) pump wave to one e/m and one electrostatic (e/s) daughter wave. In an unmagnetized plasma, this is limited to stimulated Brillouin (SBS) and Raman (SRS) scattering. In order for parametric coupling to occur, the following frequency and wave-vector matching conditions must be met:

$$\omega_0 = \omega_1 + \omega_2, \tag{2}$$

$$\vec{k}_0 = \vec{k}_1 + \vec{k}_2, \tag{3}$$

where the subscripts 0, 1, and 2 denote the pump, scattered, and plasma waves, respectively. Equations (2) and (3) are required by energy and momentum conservation, respectively. In the context of ICF, parametric processes can give rise to resonant modes which grow exponentially in the plasma and remove energy from the target.[9] Additionally, light backscattered through the optics of the experiment can cause significant damage and even be re-amplified.[10–12] Finally, electron plasma waves can generate superthermal or "hot" electrons which can pre-heat the fuel, thereby increasing the work required to compress it.[13]

By contrast, plasma-based laser amplification schemes utilize parametric processes to transfer energy from a long-duration, high-amplitude laser pump to a short, low-amplitude seed pulse. While both Raman and Brillouin amplification have been realized experimentally with some success,[14,15] Raman amplification is restricted to densities less than a quarter of the critical density and requires the seed pulse frequency to be significantly downshifted compared to the pump. Brillouin amplification can occur up to the critical density and negates the frequency downshift but has a lower growth rate.[16] Recently, a magnetized amplification scheme has been proposed, where the external magnetic field is neither parallel nor perpendicular to the pump wavevector. In this scheme, low-frequency magnetohydrodynamic waves mediate the energy transfer between the seed and pump. The advantages of this approach compared to unmagnetized Raman amplification are twofold: the pump and seed are closer in frequency, and the growth rate is higher. This method is additionally suitable for short pulse amplification and compression.[7]

Laser-driven parametric processes have been extensively researched in unmagnetized plasmas. However, the advent of experiments such as MagLIF, the possibility of magnetized experiments on the National Ignition Facility (NIF),[17–19] and proposed magnetized parametric laser amplification schemes[7] necessitate a re-examining of the impact of a magnetic field on them, which is usually neglected. This is not unexplored territory. For instance, prior work studied how an external axial B field affects Raman backscattering in a hot, inhomogeneous plasma,[20] and the decay of circularly polarized electromagnetic waves in cold, homogeneous plasma.[21] Recently, excellent theoretical work on a warm-fluid model for magnetized LPI has been done by Shi.[22] Winjum *et al.*[23] have studied SRS in a magnetized plasma with a particle-in-cell code in conditions relevant to indirect-drive ICF. This work focuses on how the B field affects large-amplitude Langmuir waves, which can nonlinearly trap resonant electrons and modify the Landau damping. Our work ignores nonlinearity and damping, both of which are important in real systems.

Besides modifying existing processes, a background B field gives rise to new waves, one of which is an electromagnetic "whistler" wave which has $\omega \leq \omega_{ce}$, the electron cyclotron frequency. Thus, a plethora of new parametric processes involving this wave can occur, including one which we call "stimulated whistler scattering" (SWS), in which the pump light wave decays to an electrostatic Langmuir wave and a whistler wave. Parametric processes involving whistlers have been known for some time. For instance, a collection of new instabilities (mostly involving whistler waves) which include purely growing, modulational and beat-wave instabilities in hot, inhomogeneous plasmas has been explored by Forslund *et al.*[24] The decay of a high-frequency whistler wave into a Bernstein wave and a low-frequency whistler wave in hot, inhomogeneous plasmas has also been investigated.[25] Additionally, parametric decays involving three whistler waves in cold, homogeneous plasmas have been studied.[26] In magnetized fusion, parametric interactions of large-amplitude RF waves launched by external antennas, for plasma heating and current drive, have been explored since the 1970s.[27]

This paper has two main objectives. First, to present the theory of magnetized LPI in a didactic and self-contained way, for a simple enough situation where that is feasible. Namely, we consider all wavevectors parallel to the background B field and use warm-fluid theory with multiple ion species. We work with left and right circularly polarized waves, a natural choice for this magnetic field configuration, which allows for Faraday rotation. We obtain the uncoupled, linear waves and a parametric dispersion relation [Eq. (67)], meaning one where the pump light wave is included in the equilibrium, in the spirit of Drake *et al.*[28] (unmagnetized) and Manheimer and Ott[29] (magnetized—but details lacking). This allows the calculation of growth rates and the inclusion of strong coupling, where the parametric coupling significantly alters the daughter waves from their linear, uncoupled dispersion relations. It also includes both frequency up- and down-shifted scattered light waves. This paper is, to our knowledge, the only published, detailed derivation of such a magnetized parametric dispersion relation.

The paper's second goal is to study magnetized LPI in HED-relevant conditions (e.g., for NIF and MagLIF). We do this via the "kinematics" of magnetized three-wave interactions, based on phase-matching of linear, uncoupled waves. This approach treats the parametric coupling as small and is, thus, a special case of prior work, especially the weakly coupled, warm-fluid model developed by Shi.[22] We quantify the effect of the imposed magnetic field on SRS and SBS spectra, which is small for fields that have been achieved on existing facilities. Analytic approximate expressions for the shifts in scattered wavelength due to the *B* field are also given. We then consider SWS, which, to the best of our knowledge, is the first such explicit analysis in the HED and LPI contexts. We believe the HED and LPI communities will find this self-contained theory and simple application to present experiments useful.

The rest of the paper is organized as follows. In Sec. II, we use the warm-fluid equations to derive the parametric dispersion relation. These are then linearized and decomposed in Fourier modes. Only resonant terms satisfying phase-matching are retained. In Sec. III, the resulting free-wave dispersion relations in a magnetized and unmagnetized plasma are discussed, along with the Faraday rotation of light-wave polarization. Section IV studies the impact of the external magnetic field on stimulated Raman and Brillouin scattering in typical HED plasmas. Stimulated whistler scattering is also explored. Section V concludes and discusses future prospects.

II. PARAMETRIC DISPERSION RELATIONS FOR MAGNETIZED PLASMA WAVES

This section develops a parametric dispersion relation, meaning one where the pump is included in the equilibrium. This approach is in the spirit of the paper by Drake *et al.*[28] for kinetic, unmagnetized plasma waves and also for magnetized waves.[29] Subsequent kinetic work was done which extended the Drake approach to include a background B field.[30,31] While our approach does not contain new results compared to the latter, we believe it is useful to work through the details explicitly—especially in a form familiar to the unmagnetized LPI community. The upshot of the lengthy math is Eq. (67), which the reader should understand in physical terms before delving into the details of this section. Our goal is expressions for the amplitude-independent Ds (which give linear dispersion relations) and Δs (which give parametric coupling).

A. Governing equations

The subscript s will be used to denote species, with mass m_s and charge $q_s = Z_s e$ ($e > 0$ the positron charge). The subscript j will denote the wave or mode. We start with the 3D, non-relativistic Vlasov–Maxwell system with no collisions and assume spatial variation only in the z direction. Hence, all vectors directed along $\hat{z}$ are longitudinal, and all vectors which lie in the x–y plane are transverse. An experimental configuration for which these assumptions hold is shown in Fig. 1. We further assume that the distribution function for species s, f_s (particles per $dz \times d^3w$, where $\vec{w}$ denotes velocity, and we have integrated over x and y) can be written in a separable form: $f_s(t,z,\vec{w}) = f_{s\perp}(t,z,\vec{w}_\perp)F_s(t,z,w_z)$. $f_{s\perp}$ allows for transverse electromagnetic waves and is normed such that $\int f_{s\perp} d^2w_\perp = 1$. F_s is the 1D distribution (particles per $dz \times dw_z$). Standard manipulations lead to the following 1D Vlasov–Maxwell system:

$$\partial_t F_s + w_z \partial_z F_s = -\frac{q_s}{m_s}(E_z + (\vec{v}_s \times \vec{B})_z)\partial_{w_z} F_s, \tag{4}$$

$$(\partial_t + v_{sz}\partial_z)\vec{v}_{s\perp} = \frac{q_s}{m_s}(\vec{E}_\perp + (\vec{v}_s \times \vec{B})_\perp), \tag{5}$$

$$n_s = \int F_s \mathrm{d}w_z, \quad \vec{v}_{s\perp} = \int f_{s\perp}\vec{w}_\perp \mathrm{d}^2w_\perp, \quad v_{sz} = n_s^{-1}\int F_s w_z \mathrm{d}w_z, \tag{6}$$

$$B_z = B_{eq} = \text{const}, \tag{7}$$

$$\partial_t \vec{B}_\perp = \partial_z(E_y, -E_x), \tag{8}$$

$$\partial_t \vec{E}_\perp = c^2\partial_z(-B_y, B_x) - \frac{e}{\varepsilon_0}\sum_s Z_s n_s \vec{v}_{s\perp}, \tag{9}$$

$$\partial_t E_z = -\frac{e}{\varepsilon_0}\sum_s Z_s n_s v_{sz}. \tag{10}$$

$B_{eq} > 0$ and the subscript eq indicates a nonzero, zeroth order background term. Poisson's equation is not listed since the inclusion of Ampère's law and charge continuity render it redundant. It is possible

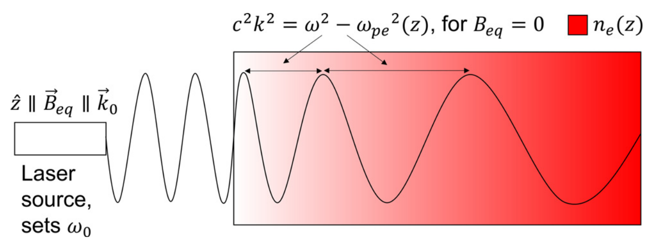

FIG. 1. Geometry of the experimental setup considered throughout the paper. The pump frequency, ω_0, is set by the laser. An external magnetic field, $B_{eq}\hat{z}$, is imposed parallel to the propagation direction of the laser, $\hat{k}_0$. The laser is incident from vacuum on a plasma with density, n_e, which varies with z. The wave vector is, therefore, also z dependent.

to satisfy Maxwell's equations [Eqs. (8)–(10)] by writing $\vec{E}$ and $\vec{B}$ in terms of scalar and vector potentials, ϕ and $\vec{A}$: $\vec{E} = -\vec{\nabla}\phi - \frac{\partial \vec{A}}{\partial t}$ and $\vec{B} = \vec{\nabla} \times \vec{A} + B_{eq}\hat{z}$. We choose the Weyl gauge in which $\phi = 0$ and $\vec{A} = \vec{A}_\perp + A_z\vec{z}$. Faraday's law is then automatic, and the remaining Maxwell's equations become

$$\partial_t^2 A_z = \frac{e}{\varepsilon_0}\sum_s Z_s n_s v_{sz}, \tag{11}$$

$$(\partial_t^2 - c^2\partial_z^2)\vec{A}_\perp = \frac{e}{\varepsilon_0}\sum_s Z_s n_s \vec{v}_{s\perp}. \tag{12}$$

We arrive at fluid equations by taking moments $\int w_z^p \mathrm{d}w_z$ of the equation for F_s, for $p = 0$, 1, and 2

$$\partial_t n_s + \partial_z(n_s v_{sz}) = 0, \tag{13}$$

$$\partial_t(n_s v_{sz}) + \partial_z\left(n_s v_{sz}^2 + \frac{P_s}{m_s}\right) = \frac{q_s n_s}{m_s}(E_z + (\vec{v}_s \times \vec{B})_z), \tag{14}$$

$$(\partial_t + v_{sz}\partial_z)P_s = -3P_s\partial_z v_{sz} - 2\partial_z Q_s \tag{15}$$

with pressure $P_s \equiv m_s \int F_s(w_z - v_{sz})^2 \mathrm{d}w_z$ and heat flux $Q_s \equiv (m_s/2) \times \int F_s(w_z - v_{sz})^3 \mathrm{d}w_z$. Note that the pressure is the zz component of the 3D pressure tensor, *not* the scalar, isotropic pressure. We can close the fluid-moment system by replacing the pressure equation with a polytrope equation of state, where K_s is a constant

$$P_s = n_s T_s = K_s n_s^{\gamma_s}, \tag{16}$$

$$\partial_z P_s = K_s\gamma_s n_s^{\gamma_s - 1}\partial_z n_s = \gamma_s T_s \partial_z n_s. \tag{17}$$

Common choices for linearized dynamics are isothermal ($\gamma_s = 1$) and adiabatic ($\gamma_s = 3$), which follows from setting $Q_s = 0$ in the pressure equation. Let us recap the complete fluid-Maxwell system, with the substitutions $\vec{a} = \frac{e}{m_e}\vec{A}$ (units of speed), $\omega_{ps}^2 = \frac{q_s^2 n_{seq}}{\varepsilon_0 m_s}$, $\omega_{cs} = |\frac{q_s}{m_s}B_{eq}|$, $\mu_s = \frac{m_s}{m_e Z_s}$, and $s_s = -1, 1$ for electrons and ions, respectively,

$$\partial_t^2 a_z - \sum_s \omega_{ps}^2 \mu_s \frac{n_s}{n_{seq}} v_{sz} = 0, \tag{18}$$

$$(\partial_t^2 - c^2\partial_z^2)\vec{a}_\perp = \sum_s \omega_{ps}^2 \mu_s \frac{n_s}{n_{seq}}\vec{v}_{s\perp}, \tag{19}$$

$$\partial_t v_{sz} + \mu_s^{-1}\partial_t a_z + v_{sz}\partial_z v_{sz} + \gamma_s\frac{T_s}{m_s n_s}\partial_z n_s = \mu_s^{-1}\vec{v}_{s\perp}\cdot\partial_z\vec{a}_\perp, \tag{20}$$

$$\partial_t\vec{v}_{s\perp} + \mu_s^{-1}\partial_t\vec{a}_\perp - s_s\omega_{cs}\vec{v}_{s\perp}\times\hat{z} = -\mu_s^{-1}v_{sz}\partial_z\vec{a}_\perp - v_{sz}\partial_z\vec{v}_{s\perp}, \tag{21}$$

$$\partial_t n_s + \partial_z(n_s v_{sz}) = 0. \tag{22}$$

Terms that can give rise to parametric couplings of interest have been moved to the RHS. These involve at least one e/m wave, which will become the pump, and one e/m or e/s wave, which will become one of the daughters. All other terms have been moved to the LHS, namely, those that are purely linear or contain second-order terms not of interest. It is clear that the longitudinal dynamics are unaffected by B_{eq} in the absence of the parametric coupling since we chose $\vec{k}||B_{eq}\hat{z}$.

B. Linearization: Physical space

We consider parametric processes involving the decay of a fixed, finite-amplitude, electromagnetic pump to an electromagnetic and an electrostatic daughter wave, denoted by subscripts 0, 1, and 2, respectively. The daughter waves are assumed to be much lower in amplitude than the pump. We write the velocity and vector potential pertaining to each wave as an infinite sum of terms of increasing order in amplitude. We neglect all terms of second order or higher in the pump amplitude (such as the ponderomotive term, which scales as a_0^2), retaining only terms which are strictly linear in wave amplitudes or involve the product of one pump and one daughter amplitude. The plasma density is approximated by the sum of a static, uniform equilibrium term, n_{seq} and a perturbation induced by the electrostatic wave, n_{s2}. We assume that no background flows exist in the plasma ($v_{seq} = 0$), no external electric fields are imposed upon it ($a_{eq} = 0$), and quasi-neutrality holds ($\sum_s q_s n_{seq} = 0$). We write

$$\vec{a}_\perp = \vec{a}_{0\perp} + \vec{a}_{1\perp}, \tag{23}$$

$$a_z = a_2, \tag{24}$$

$$\vec{v}_{s\perp} = \vec{v}_{s0\perp} + \vec{v}_{s1\perp}, \tag{25}$$

$$v_{sz} = v_{s2}, \tag{26}$$

$$n_{sz} = n_{seq} + n_{s2}, \tag{27}$$

where $\vec{a}_j$, $\vec{v}_j$, and n_{s2} are functions of t, z. Since we are only interested in second-order terms which give rise to the parametric coupling, we can linearize equation (17)

$$\frac{\partial_z P_s}{n_s} = \gamma_s \frac{T_{seq}}{n_{seq}} \partial_z n_{s2}. \tag{28}$$

Substituting these results and Eqs. (23)–(27) into Eqs. (18)–(22) and keeping only coupling terms of interest, we obtain, for waves 1 and 2,

$$\partial_t^2 a_2 - \sum_s \omega_{ps}^2 \mu_s v_{s2} = 0, \tag{29}$$

$$(\partial_t^2 - c^2 \partial_z^2)\vec{a}_1 - \sum_s \omega_{ps}^2 \mu_s \vec{v}_{s1} = \sum_s \omega_{ps}^2 \mu_s \frac{n_{s2}}{n_{seq}} \vec{v}_{s0}, \tag{30}$$

$$\partial_t v_{s2} + \mu_s^{-1} \partial_t a_2 + \gamma_s \frac{v_{Ts}^2}{n_{seq}} \partial_z n_{s2} = \mu_s^{-1}(\vec{v}_{s0} \cdot \partial_z \vec{a}_1 + \vec{v}_{s1} \cdot \partial_z \vec{a}_0), \tag{31}$$

$$\partial_t \vec{v}_{s1} + \mu_s^{-1} \partial_t \vec{a}_1 - s_s \omega_{cs} \vec{v}_{s1} \times \hat{z} = -v_{s2} \partial_z (\vec{v}_{s0} + \mu_s^{-1} \vec{a}_0), \tag{32}$$

$$\partial_t n_{s2} + n_{seq} \partial_z v_{s2} = 0, \tag{33}$$

where $v_{Ts}^2 = \frac{T_{eqs}}{m_s}$. The $-v_{sz}\partial_z v_{sz}$ term in Eq. (20) has been neglected because it is second order in the daughter wave amplitude. Wave 0 satisfies the same equations as wave 1 [i.e., Eqs. (30) and (32)] without the coupling terms (RHS = 0). For the daughter waves 1 and 2, we now have $2s+1$ scalar and $s+1$ vector equations for $2s+1$ scalar (n_{s2}, v_{s2}, and a_2) and $s+1$ vector ($\vec{v}_{s1}$ and $\vec{a}_1$) unknowns, with all vectors in the 2D transverse (xy) plane. Our plan is to move to Fourier space, retain only linear and parametric-coupling terms, and arrive at a closed system just involving the as.

C. Fourier decompositions

If the variable X is used to represent the electric field, electron density, or wave velocity, then X can be written as a Fourier decomposition, in which j denotes the wave (0,1,2)

$$X_j(t, \vec{r}) = \frac{1}{2} X_{fj} e^{i\psi_j} + \text{c.c.} \tag{34}$$

Subscript f denotes the Fourier amplitude, phase $\psi_j = (\vec{k}_j \cdot \vec{r} - \omega_j t) \equiv k_j z - \omega_j t$, and c.c. is an abbreviation of complex conjugate. Since all successive amplitudes will be Fourier amplitudes, the subscript f will, henceforth, be neglected. Wave 1 can be written in terms of two e/m waves, with either an up-shifted or a down-shifted frequency vs wave 0, denoted by subscripts + and −, respectively. The phase-matching conditions are, hence,

$$\psi_- = \psi_0 - \psi_2^*, \quad \psi_+ = \psi_0 + \psi_2. \tag{35}$$

Growth due to the parametric coupling means the daughter-wave k_j and ω_j can be complex. It is assumed that the pump amplitude is fixed (no damping or pump depletion); hence, k_0 and ω_0 are real, and $\psi_0^* = \psi_0$. We choose our definitions of $\psi_\pm$, so they and ψ_2 have the same imaginary part, i.e., the same parametric growth rate. We also choose all frequencies to have a positive real part: the companion field for $\text{Re}[\omega] < 0$ follows from the condition that the physical field is real. Although one can mix positive and negative frequency waves, we find the analysis simpler with all $\text{Re}[\omega] > 0$. Especially with magnetized waves, the discussion of circular polarization for $\text{Re}[\omega] < 0$ can become confusing.

1. Plasma waves in Fourier space

We shall eliminate n_{s2} and $\vec{v}_{s2}$ in favor of the as. Substituting Eq. (34) into Eqs. (29) and (33), we obtain

$$a_2 + \frac{1}{\omega_2^2} \sum_s \omega_{ps}^2 \mu_s v_{s2} = 0 \tag{36}$$

and

$$n_{s2} = n_{seq} \frac{k_2}{\omega_2} v_{s2}, \tag{37}$$

respectively. Repeating for Eq. (31) gives

$$\left(-\frac{\omega_2}{2} v_{s2} - \frac{\mu_s^{-1}}{2} \omega_2 a_2 + \frac{\gamma_s v_{Ts}^2}{2 n_{eqs}} k_2 n_{s2} \right) + \text{c.c.} = \frac{\mu_s^{-1}}{4} PC_{s2} + \text{c.c.}, \tag{38}$$

where the parametric coupling terms are contained in PC_{s2} (units of frequency × speed), and

$$\begin{aligned} PC_{s2} = &- ie^{-i\psi_2} \sum_{+,-} Res_2 \Big[(\vec{v}_{s0} e^{i\psi_0}) \cdot (ik_\pm \vec{a}_\pm e^{i\psi_\pm}) \\ &+ (\vec{v}_{s0} e^{i\psi_0}) \cdot (-ik_\pm^* \vec{a}_\pm^* e^{-i\psi_\pm^*}) + (\vec{v}_{s\pm} e^{i\psi_\pm}) \cdot (ik_0 \vec{a}_0 e^{i\psi_0}) \\ &+ (\vec{v}_{s\pm} e^{i\psi_\pm}) \cdot (-ik_0^* \vec{a}_0^* e^{-i\psi_0^*}) + \text{c.c.} \Big], \end{aligned} \tag{39}$$

where Res_2 denotes terms which are resonant with mode 2. Using Eq. (37) to substitute for n_{s2}

$$-\omega_2 (v_{s2} + \mu_s^{-1} a_2) + \gamma_s \frac{k_2^2 v_{Ts}^2}{\omega_2} v_{s2} = \frac{\mu_s^{-1}}{2} PC_{s2}. \tag{40}$$

Rearranging for v_{s2},

$$v_{s2} = -\frac{\omega_2 P_s}{\mu_s \omega_{ps}^2} (\omega_2 a_2 + PC_{s2}), \tag{41}$$

$$P_s = \frac{\omega_{ps}^2}{\omega_2^2 - \gamma_s k_2^2 v_{Ts}^2}. \tag{42}$$

Substituting this result into Eq. (36), we obtain

$$\left(1-\sum_s P_s\right)a_2=\frac{1}{2\omega_2}\sum_s P_sPC_{s2}\,. \tag{43}$$

2. EM waves in Fourier space

Writing Eq. (32) in terms of Fourier modes, we obtain

$$\begin{aligned}\frac{1}{2}\sum_{+,-}&\left(-i\omega_\pm\vec{v}_{s\pm}-i\mu_s^{-1}\omega_\pm\vec{a}_\pm-s_s\omega_{cs}\vec{v}_{s\pm}\times\hat{z}\right)e^{i\psi_\pm}+\text{c.c.}\\ &=-\frac{1}{4}\left[ik_0v_{s2}\vec{v}_{s0}e^{i\psi_+}+ik_0v_{s2}^*\vec{v}_{s0}e^{i\psi_-}\right.\\ &\quad\left.+\mu_s^{-1}\left(ik_0v_{s2}\vec{a}_0e^{i\psi_+}+ik_0\vec{a}_0v_{s2}^*e^{i\psi_-}\right)\right]+\text{c.c.}\end{aligned} \tag{44}$$

Let Z_{y+}, Z_{y-} denote Z_y and Z_y^*, respectively, where Z denotes an amplitude, frequency, or wavelength, and y denotes a subscript containing the mode and plasma species (if applicable) of Z. This allows us to write generic equations for the $+$ and $-$ waves. Selecting only resonant terms, we obtain

$$\omega_\pm(\vec{v}_{s\pm}+\mu_s^{-1}\vec{a}_\pm)-is_s\omega_{cs}\vec{v}_{s\pm}\times\hat{z}=\frac{k_0}{2}v_{s2\pm}(\vec{v}_{s0}+\mu_s^{-1}\vec{a}_0)\,. \tag{45}$$

Finally, Eq. (30), once written in terms of Fourier modes, becomes

$$\begin{aligned}\frac{1}{2}\sum_{+,-}&\left((-\omega_\pm^2+c^2k_\pm^2)\vec{a}_\pm-\sum_s\omega_{ps}^2\mu_s\vec{v}_\pm\right)e^{i\psi_\pm}+\text{c.c.}\\ &=\sum_s\omega_{ps}^2\frac{\mu_s}{4n_{seq}}\left(\vec{v}_{s0}n_{s2}e^{i\psi_+}+\vec{v}_{s0}n_{s2}^*e^{i\psi_-}\right)+\text{c.c.}\end{aligned} \tag{46}$$

Keeping terms resonant with $\psi_\pm$ and eliminating n_{s2} gives

$$(-\omega_\pm^2+k_\pm^2c^2)\vec{a}_\pm-\sum_s\omega_{ps}^2\mu_s\vec{v}_{s\pm}=\frac{1}{2}\frac{k_{2\pm}}{\omega_{2\pm}}\sum_s\omega_{ps}^2\mu_sv_{s2\pm}\vec{v}_{s0}. \tag{47}$$

Using Eq. (41) to eliminate v_{s2} from Eqs. (45) and (47), keeping only terms up to second order, we are left with the following equations, where we restate the plasma-wave equation for convenience

$$\vec{v}_{s\pm}+\mu_s^{-1}\vec{a}_\pm-i\beta_{s\pm}\vec{v}_{s\pm}\times\hat{z}=-K_{s\pm}a_{2\pm}(\vec{v}_{s0}+\mu_s^{-1}\vec{a}_0)\,, \tag{48}$$

$$(-\omega_\pm^2+k_\pm^2c^2)\vec{a}_\pm-\sum_s\omega_{ps}^2\mu_s\vec{v}_{s\pm}=-\frac{k_{2\pm}\omega_{2\pm}}{2}\sum_s P_{s\pm}a_{2\pm}\vec{v}_{s0}, \tag{49}$$

$$(1-\sum_s P_s)a_2=\frac{1}{2\omega_2}\sum_s P_sPC_{s2}. \tag{50}$$

$K_{s\pm}=\frac{k_0\omega_{2\pm}^2P_{s\pm}}{2\mu_s\omega_\pm\omega_{ps}^2}$, $\beta_{s\pm}=s_s\frac{\omega_{cs}}{\omega_\pm}$, and $P_{s\pm}=\frac{\omega_{ps}^2}{\omega_{2\pm}^2-\gamma_sk_{2\pm}^2v_{Ts}^2}$. $\omega_{2+}=\omega_2$, $\omega_{2-}=\omega_2^*$, and similarly for $k_{2\pm}$. The equations for wave 0 are equivalent to those for the $\pm$ waves, neglecting second-order terms.

At this point, the remaining task is to solve for $\vec{v}_{s\pm}$ in terms of $\vec{a}_\pm$, a_2, and wave 0 quantities. We will finally arrive at a 5×5 system for $\vec{a}_+$, $\vec{a}_-^*$, and a_2, which includes both the linear waves and parametric coupling to wave 0. For magnetized waves, this is most easily done in a rotating coordinate system, where R and L circularly polarized waves are the linear light waves.

D. Left–right co-ordinate system

It is convenient when dealing with Fourier amplitudes to formulate vectors in terms of right- and left-polarized co-ordinates, which are defined in terms of Cartesian coordinates as follows:

$$\begin{aligned}\hat{R}&=\frac{1}{\sqrt{2}}(\hat{x}+i\hat{y}),\\ \hat{L}&=\frac{1}{\sqrt{2}}(\hat{x}-i\hat{y}).\end{aligned} \tag{51}$$

In condensed notation,

$$\hat{\sigma}=\frac{1}{\sqrt{2}}(\hat{x}+i\sigma\hat{y}), \tag{52}$$

where $\sigma=+1,-1$ for the right- and left-polarized basis vectors, respectively. We define the dot product such that $\vec{a}\cdot\vec{b}=\sum_i a_ib_i^*$. Thus, dot products do not commute: $\vec{a}\cdot\vec{b}=(\vec{b}\cdot\vec{a})^*$. This normalization ensures $\hat{\sigma}\cdot\hat{\sigma}=1$. Using this convention, any vector can be re-written in terms of right- and left-polarized unit vectors and amplitudes. Consider, for example, the physical velocity vector $\vec{v}_\perp$, where we explicitly indicate Fourier amplitudes with subscript f

$$\begin{aligned}\vec{v}_\perp&=(\hat{x}v_{fx}+\hat{y}v_{fy})e^{i\psi}+\text{c.c.}\\ &=\frac{1}{\sqrt{2}}((\hat{R}+\hat{L})v_{fx}+i(\hat{L}-\hat{R})v_{fy})e^{i\psi}+\text{c.c.}\\ &=\frac{1}{\sqrt{2}}(\hat{L}(v_{fx}+iv_{fy})+\hat{R}(v_{fx}-iv_{fy}))e^{i\psi}+\text{c.c.}\\ &=\frac{1}{\sqrt{2}}(v_{fL}\hat{L}+v_{fR}\hat{R})e^{i\psi}+\text{c.c.}\\ &=e^{i\psi}\sum_\sigma v_{f\sigma}\hat{\sigma}+\text{c.c.}\end{aligned} \tag{53}$$

Note that $\vec{v}\cdot\hat{\sigma}=2^{-1/2}e^{i\psi}(v_x-i\sigma v_y)=e^{i\psi}v_{f\sigma}+\text{c.c.}$ As an explicit example, for an R wave with $v_{fR}=V$ real and $v_{fL}=0$, $\vec{v}_\perp=2^{1/2}V(\cos\psi,-\sin\psi)$. At fixed z, $\vec{v}_\perp$ rotates clockwise as time increases when looking toward $-\hat{z}$, which is opposite to $\vec{B}_{eq}$. We, therefore, follow the convention used by Stix,[32] in which circular polarization is defined relative to $\vec{B}_{eq}$ and not $\vec{k}$.

We use the result given in the last line of Eq. (53) to produce the definition of a dot product of two vectors in Fourier space in this coordinate system. Consider the vectors $\vec{v}$ and $\vec{a}$

$$\vec{v}.\vec{a}=e^{i(\psi_i-\psi_j^*)}(v_{fRi}a_{fRj}^*+v_{fLi}a_{fLj}^*)+\text{c.c.}, \tag{54}$$

where the subscripts i, j are the wave indices.

E. EM waves in left–right coordinates

Taking $\hat{\sigma}\cdot$ [Eqs. (48) and (49)], we obtain

$$(1+\sigma\beta_{s\pm})v_{s\pm\sigma}+\mu_s^{-1}a_{\pm\sigma}=-K_{s\pm}\left(\mu_s^{-1}a_{0\sigma}+v_{s0\sigma}\right)a_{2\pm}\,, \tag{55}$$

$$(\omega_\pm^2-k_\pm^2c^2)a_{\pm\sigma}+\sum_s\omega_{ps}^2\mu_sv_{s\pm\sigma}=\frac{k_{2\pm}\omega_{2\pm}}{2}\sum_s P_{s\pm}a_{2\pm}v_{s0\sigma}, \tag{56}$$

respectively, where $a_{\pm\sigma}\equiv\vec{a}_\pm\cdot\hat{\sigma}$. The definitions of $v_{s\pm\sigma}$, $v_{s0\sigma}$, and $a_{0\sigma}$ are analogous to that of $a_{\pm\sigma}$. We now have uncoupled equations for $(a_{\pm\sigma}, v_{s\pm\sigma})$ which is the advantage of using rotating coordinates. This is unlike the original x and y coordinates, which are coupled due to the $\vec{v}\times\vec{B}$ force. For the pump wave, we have these equations with subscript $\pm\to0$ and set the RHS to 0. Thus,

$$v_{s0\sigma}=-\frac{1}{\mu_s(1+\sigma\beta_{s0})}a_{0\sigma}. \tag{57}$$

Rearranging Eq. (55) to obtain an expression for $v_{s\pm\sigma}$

$$(1+\sigma\beta_{s\pm})v_{s\pm\sigma} = -\mu_s^{-1}a_{\pm\sigma} - \frac{\sigma K_{s\pm}\beta_{s0}}{\mu_s(1+\sigma\beta_{s0})}a_{0\pm\sigma}a_{2\pm}. \tag{58}$$

Substituting this into Eq. (56) and moving parametric coupling terms to the right-hand side, we obtain

$$D_{\pm\sigma}a_{\pm\sigma} = -\Delta_{\pm\sigma 2}a_{0\sigma}a_{2\pm}, \tag{59}$$

where

$$\begin{aligned} D_{\pm\sigma} &= \omega_\pm^2 - k_\pm^2 c^2 - \textstyle\sum_s \frac{\omega_{ps}^2}{1+\sigma\beta_{s\pm}}, \\ \Delta_{\pm\sigma 2} &= \frac{\omega_{2\pm}}{2}\sum_s \frac{P_{s\pm}}{\mu_s}\frac{1}{1+\sigma\beta_{s0}}\left(k_{2\pm} - k_0\frac{\omega_{2\pm}}{\omega_\pm}\frac{\sigma\beta_{s0}}{1+\sigma\beta_{s\pm}}\right). \end{aligned} \tag{60}$$

This has the desired form, where wave amplitudes are written only in terms of as, not vs. For no B field, all βs are zero, and the parametric coupling coefficient $\Delta_{\pm\sigma 2} \propto k_{2\pm}$, the usual unmagnetized result. To explain the notation, D_{+R} gives the linear dispersion relation for the scattered upshifted R wave, and Δ_{+R2} is the parametric coupling coefficient for that wave and wave 2 (the plasma wave). Please see the parametric dispersion relation equation (67).

F. Plasma waves in left-right coordinates

Writing the PC_{s2} term in Eq. (50) in terms of right and left circularly polarized waves, we obtain

$$\begin{aligned} PC_{s2} = &-k_-^*(v_{s0R}a_{-R}^* + v_{s0L}a_{-L}^*) + k_0(v_{s-R}^*a_{0R} + v_{s-L}^*a_{0L}) \\ &+ k_+(v_{s0R}^*a_{+R} + v_{s0L}^*a_{+L}) - k_0(v_{s+R}a_{0R}^* + v_{s+L}a_{0L}^*). \end{aligned} \tag{61}$$

Substituting for $\vec{v}_{s0}$ using Eq. (57), and $\vec{v}_{s\pm}$ using Eq. (58)

$$\begin{aligned} -\mu_s PC_{s2} = &a_{0R}a_{-R}^*\left(\frac{k_0}{1+\beta_{s-}^*} - \frac{k_-^*}{1+\beta_{s0}}\right) \\ &+ a_{0L}a_{-L}^*\left(\frac{k_0}{1-\beta_{s-}^*} - \frac{k_-^*}{1-\beta_{s0}}\right) \\ &+ a_{0R}^*a_{+R}\left(-\frac{k_0}{1+\beta_{s+}} + \frac{k_+}{1+\beta_{s0}}\right) \\ &+ a_{0L}^*a_{+L}\left(-\frac{k_0}{1-\beta_{s+}} + \frac{k_+}{1-\beta_{s0}}\right). \end{aligned} \tag{62}$$

Equation (50) can now be written in a more condensed form

$$D_2 a_2 = -\sum_\sigma(\Delta_{2+\sigma}a_{0\sigma}^*a_{+\sigma} + \Delta_{2-\sigma}a_{0\sigma}a_{-\sigma}^*), \tag{63}$$

$$D_2 = 1 - \sum_s P_s, \tag{64}$$

$$\Delta_{2+\sigma} = \frac{1}{2\omega_2}\sum_s \frac{P_s}{\mu_s}\left(\frac{k_+}{1+\sigma\beta_{s0}} - \frac{k_0}{1+\sigma\beta_{s+}}\right), \tag{65}$$

$$\Delta_{2-\sigma} = \frac{1}{2\omega_2}\sum_s \frac{P_s}{\mu_s}\left(-\frac{k_-^*}{1+\sigma\beta_{s0}} + \frac{k_0}{1+\sigma\beta_{s-}^*}\right). \tag{66}$$

We now have a plasma–wave relation involving just as.

G. Parametric dispersion relation

Equations (59) [really four equations: Eq. (59) and its complex conjugate for $\sigma = R, L$] and (63) form a system of five linear equations, which can be summarized in matrix form

$$\begin{bmatrix} D_{+R} & 0 & 0 & 0 & \Delta_{+R2}a_{0R} \\ 0 & D_{-R}^* & 0 & 0 & \Delta_{-R2}^*a_{0R}^* \\ 0 & 0 & D_{+L} & 0 & \Delta_{+L2}a_{0L} \\ 0 & 0 & 0 & D_{-L}^* & \Delta_{-L2}^*a_{0L}^* \\ \Delta_{2+R}a_{0R}^* & \Delta_{2-R}a_{0R} & \Delta_{2+L}a_{0L}^* & \Delta_{2-L}a_{0L} & D_2 \end{bmatrix}\begin{bmatrix} a_{+R} \\ a_{-R^*} \\ a_{+L} \\ a_{-L^*} \\ a_2 \end{bmatrix} = 0. \tag{67}$$

The structure of this matrix matches our physical understanding of plasma–wave dispersion relations: the diagonal terms are independent of a and give rise to linear waves. The off diagonal terms are all proportional to a_0 and represent the parametric coupling between the e/m and e/s (plasma) daughter waves. Nonzero solutions exist when the determinant is zero, which gives the parametric dispersion relation including the pump light wave in the equilibrium. This is analogous to Drake *et al.*,[28] but generalized to include a background magnetic field, and specialized to our 1D geometry and fluid instead of a kinetic plasma–wave response. It should also be a special case of the magnetized results in Manheimer and Ott,[29] which we find difficult to penetrate. One could also derive parametric growth rates from Eq. (67) and compare to those of Shi.[22] We defer this to future work since we do not use growth rates in the subsequent application to HED conditions.

The parametric dispersion relation couples a pump and scattered e/m wave of the same R or L polarization. Consider the case where there is only one pump wave: i.e., either $a_{0R} = 0$ or $a_{0L} = 0$. Taking $a_{0R} = 0$ for definiteness, waves a_{-R} and a_{-R}^* decouple from the dispersion relation, leaving the following dispersion matrix:

$$\begin{bmatrix} D_{+L} & 0 & \Delta_{+L2}a_{0L} \\ 0 & D_{-L}^* & \Delta_{-L2}^*a_{0L}^* \\ \Delta_{2+L}a_{0L}^* & \Delta_{2-L}a_{0L} & D_2 \end{bmatrix}\begin{bmatrix} a_{+L} \\ a_{-L}^* \\ a_2 \end{bmatrix} = 0. \tag{68}$$

Setting the determinant to 0 gives

$$D_{+L}D_{-L}^*D_2 = |a_{0L}|^2(D_{+L}\Delta_{2-L}\Delta_{-L2}^* + D_{-L}^*\Delta_{2+L}\Delta_{+L2}). \tag{69}$$

$a_{0L} = 0$ then gives the three linear dispersion relations for the upshifted L, downshifted L, and plasma waves: $D_{+L} = 0$, $D_{-L} = 0$, or $D_2 = 0$. $a_{0L} \neq 0$ couples the linear waves and gives parametric interaction.

III. IMPACT OF EXTERNAL B FIELD ON FREE WAVES

This section considers the linear or free waves, with $a_0 = 0$. Let a_1 be either a_+ or a_- in Eq. (67) to obtain the free-wave dispersion relation

$$\begin{bmatrix} D_{1L}^* & 0 & 0 \\ 0 & D_{1R}^* & 0 \\ 0 & 0 & D_2 \end{bmatrix}\begin{bmatrix} a_{1L}^* \\ a_{1R}^* \\ a_2 \end{bmatrix} = 0. \tag{70}$$

$\vec{a} \neq 0$ solutions exist if the determinant of this matrix equals 0. This gives rise to the following dispersion relations, for a single ion species. For the e/m waves, with $a_2 = 0$, we have $D_{1L}D_{1R} = 0$, which gives

$$\omega_1^2 = k_1^2c^2 + \frac{\omega_{pe}^2}{1-\sigma\frac{\omega_{ce}}{\omega_1}} + \frac{\omega_{pi}^2}{1+\sigma\frac{\omega_{ci}}{\omega_1}}. \tag{71}$$

For e/s waves, with $a_{1L} = a_{1R} = 0$, we have $D_2 = 0$ and

$$\omega_2^2 = \frac{\omega_{pe}^2}{1 - \gamma_e \frac{k_2^2 v_{Te}^2}{\omega_2^2}} + \frac{\omega_{pi}^2}{1 - \gamma_i \frac{k_2^2 v_{Ti}^2}{\omega_2^2}}. \tag{72}$$

Note that the background B field has no effect at all on the e/s waves, for our geometry of $\vec{k}||\vec{B}_{eq}$.

A. Waves in an unmagnetized plasma

By setting $\omega_{ce} = 0$, we recover the unmagnetized dispersion relation for electromagnetic waves from Eq. (71)

$$\omega_1^2 = c^2 k_1^2 + \omega_{pe}^2 + \omega_{pi}^2. \tag{73}$$

The ion contribution is usually negligible. Equation (72) gives the electrostatic waves, with the conventional approximations, like neglecting ions for electron plasma waves (EPWs), being highly accurate. Namely, we find the EPW for $\gamma_e = 3$

$$\omega_2^2 = \omega_{pe}^2 + 3 v_{Te}^2 k_2^2 \tag{74}$$

and the ion acoustic wave (IAW) for $\gamma_e = 1, \gamma_i = 3$

$$\omega_2^2 = \frac{Z_i T_e}{m_i} \left(\frac{1}{1 + (k_2 \lambda_{De})^2} + \frac{3 T_i}{Z_i T_e} \right) k_2^2 \tag{75}$$

with $\lambda_{De} \equiv v_{Te}/\omega_{pe}$. We must retain finite T_e for an IAW to exist.

B. Waves with magnetic field

The dispersion relation for free electromagnetic waves in a magnetized plasma is given in Eq. (71). As is usual in LPI literature, we view this as giving ω as a function of real k. This gives a fourth-order polynomial for ω with four real solutions, each of which corresponds to an e/m wave

$$\begin{aligned}&\omega^4 - \sigma(\omega_{ce} - \omega_{ci})\omega^3 - (c^2 k^2 + \omega_{ce}\omega_{ci} + \omega_{pe}^2 + \omega_{pi}^2)\omega^2 \\ &+ \sigma(\omega_{ce} - \omega_{ci}) c^2 k^2 \omega + \omega_{ce}\omega_{ci} c^2 k^2 = 0.\end{aligned} \tag{76}$$

Note one can solve this trivially in closed form for k given ω. In the following analysis, but not in the numerical solutions, we assume $Z_i m_e/m_i \ll 1$, so we can drop ω_{pi}^2 and set $\omega_{ce} - \omega_{ci} \to \omega_{ce}$. In order of descending frequency, these waves are the right- and left-polarized light waves, the whistler wave, and the ion cyclotron wave (ICW). In addition to these waves, two electrostatic waves are obtained by solving Eq. (72): the EPW and the IAW.

Let us consider the high-frequency e/m waves, the light and whistler waves, where ion motion can be neglected: $\omega_{ci} \to 0$. In this case, Eq. (76) becomes (removing one $\omega = 0$ root)

$$\omega^3 - \sigma\omega_{ce}\omega^2 - (c^2 k^2 + \omega_{pe}^2)\omega + \sigma\omega_{ce} c^2 k^2 = 0. \tag{77}$$

We assume $\omega_{pe} \gg \omega_{ce}$, which is typical in the HED regime. For light waves, we consider Eq. (77) for $\omega \gg \omega_{ce}$. For $k = 0$, we find

$$\omega(k = 0) \approx \omega_{pe} + \frac{\sigma}{2}\omega_{ce}. \tag{78}$$

For all k, we write ω as $\omega(B_{eq} = 0) \equiv (c^2 k^2 + \omega_{pe}^2)^{1/2}$ plus a correction

$$\omega \approx \omega(B_{eq} = 0) + \frac{\sigma}{2} \frac{\omega_{pe}^2}{\omega(B_{eq} = 0)^2} \omega_{ce}. \tag{79}$$

1. Whistler wave

We can also solve Eq. (77) for the whistler wave, which has $\omega \le \omega_{ce}$. We call this full set of roots for ω the whistler though some authors only use this term for the small k domain and "electron cyclotron wave" when ω is near ω_{ce}. We derive expressions for this wave by considering two limits: first, for $k \to 0$ (but still large enough that we can neglect ion motion, discussed below), we obtain

$$\omega \approx \sigma \frac{c^2 k^2}{\omega_{pe}^2} \omega_{ce}. \tag{80}$$

We restrict interest to $\omega > 0$ waves, which for the whistler requires the R wave ($\sigma = 1$)

$$\omega \approx \frac{c^2 k^2}{\omega_{pe}^2} \omega_{ce}, \quad \sigma = 1. \tag{81}$$

Second, for $ck \gg \omega_{pe}$, we obtain

$$\omega \approx \omega_{ce} \left(1 - \frac{\omega_{pe}^2}{c^2 k^2} \right), \quad \sigma = 1. \tag{82}$$

For ω near ω_{ce}, the whistler group velocity $d\omega/dk$ approaches zero. Since this is the relevant wave propagation speed for three-wave interactions, such a localized whistler wavepacket would propagate very slowly. This impacts how stimulated whistler scattering evolves and how to practically realize the process in experiments or simulations.

The full numerical solutions of the dispersion relations for the whistler wave and the right- and left-polarized light waves are shown in Fig. 2(a). Note that here and throughout the rest of the paper, λ_{De} is used to normalize k, as is customary for stimulated scattering. For large $k\lambda_{De}$, the whistler wave tends to $\omega = \omega_{ce}$, shown in Fig. 2(a) as a dashed black line.

2. Ion cyclotron wave

We now consider the ICW which requires the retention of terms involving ion motion. As with the whistler wave, we consider two regimes. For $k \to 0$, we seek solutions with $\omega \propto k$, which gives

$$\omega \approx v_A k, \quad \sigma = -1 \quad \text{or} \quad +1, \tag{83}$$

where the Alfvén velocity, $v_A = c\frac{\omega_{ci}}{\omega_{pi}} = B/(\rho\mu_0)^{1/2}$. This solution applies for both values of σ, meaning there is both an R wave (the whistler, including ion motion) and an L wave (the ICW). To see which is which, we need to take the opposite limit $ck \gg \omega_{pe}$, where we obtain two solutions with ω independent of k: $\omega = \omega_{ce}$ for $\sigma = 1$ (the right-polarized whistler), and $\omega = \omega_{ci}$ for $\sigma = -1$ (the left-polarized ICW). Including the next correction term for the ICW gives

$$\omega \approx \omega_{ci} \left(1 - \frac{\omega_{pi}^2}{c^2 k^2} \right), \quad \sigma = 1. \tag{84}$$

Figure 2(a) is re-plotted in Fig. 2(b) for $\omega \ll \omega_{pe}$ to show the IAW and ICW clearly. The ICW tends to $\omega = \omega_{ci}$, denoted by a dashed black line. The numerical and approximate analytic solutions to the

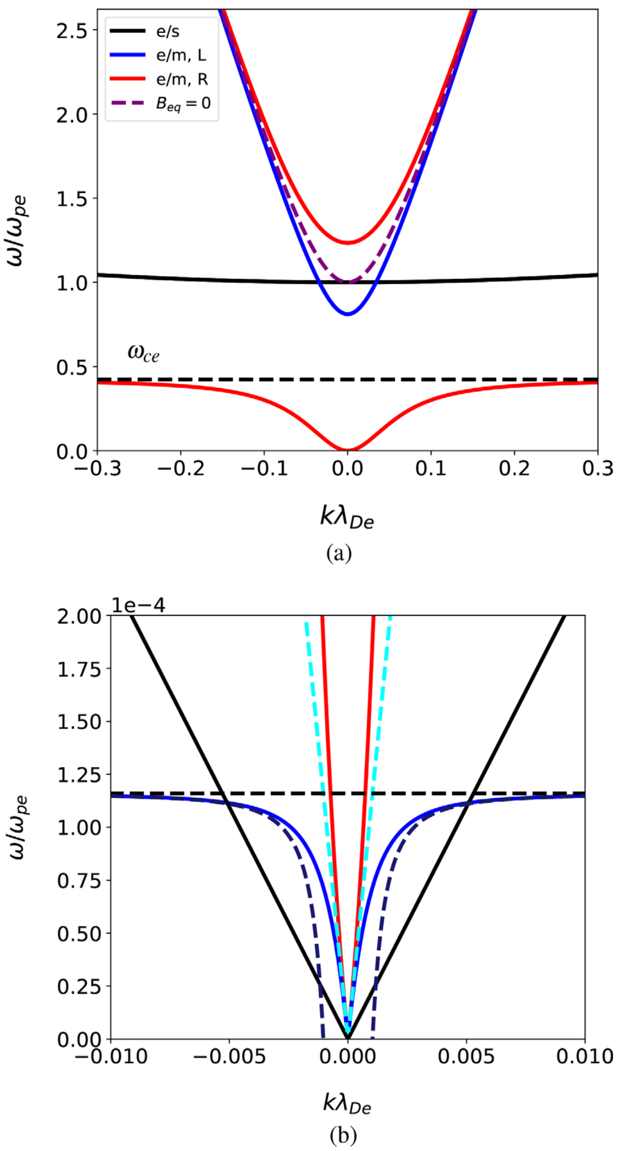

FIG. 2. Numerical solutions to the free-wave dispersion relations in a magnetized plasma, for the conditions in Table I. Red: right-polarized e/m, blue: left-polarized e/m, purple: unmagnetized e/m, and black: electrostatic. (a) High-frequency waves, in decreasing order: e/m light, electron plasma, and whistler. The black dashed line lies at $\frac{\omega_{ce}}{\omega_{pe}}$. (b) Low-frequency waves: electrostatic ion acoustic wave, right-polarized whistler, and left-polarized ion cyclotron waves. Also plotted are the analytic approximations to the ion cyclotron wave for $ck \gg \omega_{pe}$ (dark blue) [Eq. (84)], which tends to $\frac{\omega_{ci}}{\omega_{pe}}$ (dashed black line), and $k \to 0$, which yields the Alfvén frequency (dashed cyan line), given in Eq. (83).

ICW dispersion relation are shown in Fig. 2(b) in blue and dark blue, respectively. As can be seen from Eq. (83), at low $k\lambda_{De}$, the ICW approaches the Alfvén frequency, which is represented by a dashed cyan line in Fig. 2(b). For large values of $k\lambda_{De}$, the ICW frequency tends to ω_{ci}, marked by a dashed black line. The parameters used to plot the dispersion relations shown in Figs. 2(a) and 2(b) are given in Table I. A plasma comprising helium ions and electrons was considered.

TABLE I. Parameters used to plot dispersion relations.

Quantity	Value
Z	2
A	4
T_e	2 keV
T_i	1 keV
$\frac{\omega_{ce}}{\omega_{pe}}$	0.423

C. Faraday rotation

Three unique waves exist in an unmagnetized plasma, of which two are electrostatic (the electron plasma wave, EPW and the ion acoustic wave, IAW) and one is electromagnetic (light wave, with two degenerate polarizations). If the electromagnetic wave is linearly polarized, it can be written as the sum of two circularly polarized waves of equal amplitude and opposite handedness (R and L waves). If an external B field, $\vec{B_{eq}}$ is applied, the R and L waves experience different indices of refraction and propagate with differing phase velocities. Consequently, the overall polarization of the electromagnetic wave, found by summing the R and L waves, rotates as the electromagnetic wave propagates through the plasma. This is the well-known Faraday effect, which is briefly derived below.

An expression for the wavenumber of the electromagnetic wave can be obtained by rearranging Eq. (71),

$$k_\sigma = \frac{\omega}{c}\left(1 - \frac{\omega_{pe}^2}{\omega^2\left(1 - \sigma\frac{\omega_{ce}}{\omega}\right)}\right)^{\frac{1}{2}}. \tag{85}$$

Two first-order Taylor expansions of Eq. (85), assuming $\omega \gg \omega_{ce}$ and $\omega \gg \omega_{pe}$ yield

$$k_\sigma \approx K - \sigma\Delta K, \tag{86}$$

where

$$K = \frac{\omega}{c}\left(1 - \frac{\omega_{pe}^2}{2\omega^2}\right), \quad \Delta K = \frac{\omega_{pe}^2}{2\omega^2}\frac{\omega_{ce}}{c}. \tag{87}$$

Consider a linearly polarized plane electromagnetic wave. We can write the physical electric field $\vec{E} = Re[\vec{E}_F]$ as the sum of the electric fields of two circularly polarized waves with opposite handedness

$$\vec{E}_F = \varepsilon(\hat{R}e^{i\psi_R} + \hat{L}e^{i\psi_L}), \quad \psi_{R,L} \equiv k_{R,L}z - \omega t. \tag{88}$$

Writing this in Cartesian co-ordinates,

$$\frac{2^{1/2}}{\varepsilon}\vec{E}_F = \hat{x}(e^{i\psi_L} + e^{i\psi_R}) + i\hat{y}(e^{i\psi_L} - e^{i\psi_R}). \tag{89}$$

Assuming ε is real,

$$\begin{aligned} \vec{E} &= E(\cos\phi, -\sin\phi), \\ E &= |2^{1/2}\varepsilon\cos[(1/2)(k_L + k_R)z - \omega t]|, \\ \phi &= \frac{1}{2}(k_L - k_R)z = \Delta K z. \end{aligned} \tag{90}$$

TABLE II. Summary of parametric processes we study. L, R refer to left-, right-polarized e/m waves.

Process	Pump e/m wave	Scattered e/m wave	Plasma wave	Geometries (c_1, c_2)	ω_1 range	n_e/n_{crit} range
SRS	R,L	R,L	EPW	(1,1) (−1, 1)	$>\omega_{pe}$	$<1/4$
SBS	R,L	R,L	IAW	(1,1) (−1, 1)	$\gtrsim \omega_0 - \omega_{pi}$	<1
SWS	R	R-whistler	EPW	(1,−1) (−1, 1)	$<\omega_{ce}$	$\gtrsim (1-\omega_{ce}/\omega_0)^2$ for $T_e = 0$

At a fixed z, $\vec{E}$ always lies along the same line in the xy plane, with its exact position varying in time. As z varies, the angle ϕ this line makes with respect to the x axis increases at the rate

$$\frac{\partial \phi}{\partial z} = \Delta K = 16.8\,\frac{n_e}{n_{crit}} B_{eq}(\mathrm{T})(\mathrm{deg/mm}). \tag{91}$$

The final formula is in practical units. We have introduced the critical density $n_{crit} \equiv (\varepsilon_0 m_e/e^2)\omega^2$, which is the usual definition for the unmagnetized plasma. When discussing LPI, n_{crit} is for the pump wave ω_0. Significant Faraday rotation is, thus, possible in current ICF platforms with modest B fields. For instance, with $n_e/n_{crit} = 0.1$ and $B_{eq} = 10\,\mathrm{T}$, we obtain $\partial_z \phi = 16.8°/\,\mathrm{mm}$. This could be used to diagnose n_e (a common technique when feasible) and could affect LPI processes such as crossed-beam energy transfer.[33–35]

IV. IMPACT OF EXTERNAL B FIELD ON THE PARAMETRIC COUPLING

We apply the above theory to magnetized LPI in HED relevant conditions, all for $\vec{k}||\vec{B_{eq}}||\hat{z}$. We consider how the imposed field modifies SRS and SBS as well as SWS which only occurs in a background field. Recall $\vec{k}_i = k_i\hat{z}$, and we choose $k_0 > 0$. k_1 and k_2 can have either sign. Let $c_i = \mathrm{sign}(k_i)$ for $i = 1, 2$. For all three parametric processes we discuss, "forward scatter" refers to the case where the scattered e/m wave propagates in the same direction as the pump ($c_1 = +1$), and "backward scatter" to the opposite case ($c_1 = -1$). To satisfy k matching, we cannot have both $c_1 = -1$ and $c_2 = -1$. For SRS and SBS, c_2 must equal $+1$, but for SWS, $c_2 = -1$ is possible.

We do not consider growth rates but focus instead on the kinematics of three-wave interactions, through the phase-matching conditions among free waves. We study the scattered e/m wave frequency ω_1 since this is what escapes the plasma and is measured experimentally. As discussed in Sec. III C, $\vec{B_{eq}}$ causes the R and L waves to propagate with different phase velocities. Therefore, a laser or other external source that imposes a linearly polarized light wave of frequency ω_0 couples to an R and L wave in a magnetized plasma. For stimulated scattering, we are mostly interested in down-shifted scattered waves for which $\omega_1 < \omega_0$, which have the same polarization as the pump: an R or L pump couples to a down-shifted R or L scattered wave, respectively; hence, $\sigma_1 = \sigma_0$ which we, sometimes, denote as σ. We discuss SRS and SBS, which can be driven by either an R or L pump, and SWS, which can only be driven by an R pump (since the whistler wave is an R wave). Table II summarizes the processes we study.

In order to derive a dispersion relation for ω_1 in terms of known inputs, we begin with the identity $k_2 = k_2$. We use k matching to write $k_2 = k_0 - k_1$ on the left side, and the plasma–wave dispersion relation of interest to rewrite the right side in terms of ω_2. We then use the e/m dispersion relation to write k_1 in terms of ω_1 and use ω matching to write $\omega_2 = \omega_0 - \omega_1$. For SRS and SWS, this yields $k_0 - k_1 = (\omega_2^2 - \omega_{pe}^2)^{1/2}/v_{Te}3^{1/2}$. The same method is applied for SBS, where k_2 is written in terms of ω_2 using the simple IAW dispersion relation, $\omega_2 = c_s|k_2|$, for an approximate analysis (the numerical roots use the full e/s dispersion relation). That is, $c_s^2 = (Z_iT_e/m_i)\ (1 + 3T_i/Z_iT_e)$. The resulting dispersion relations can be summarized as follows:

$$\begin{aligned} M_Y \equiv &(1 - \Omega_{pe}^2(1 - \sigma_0\Omega_{ce})^{-1})^{1/2} \\ &- c_1\Omega_1(1 - \Omega_1^{-2}\Omega_{pe}^2(1 - \sigma_1\Omega_{ce}/\Omega_1)^{-1})^{1/2} - P_Y = 0, \end{aligned} \tag{92}$$

where Y is either RW, for SRS and SWS, or B, for SBS. For SRS and SWS, $P_Y = P_{RW} = c_2 V_e^{-1}((1-\Omega_1)^2 - \Omega_{pe}^2)^{1/2}$, where $V_e \equiv v_{Te}3^{1/2}/c$. For SBS, $P_Y = P_B = V_s^{-1}(1 - \Omega_1)$, with $V_s \equiv c_s/c$. This is usually very small, with 10^{-3} a typical magnitude. $\Omega_X \equiv \omega_X/\omega_0$, where X denotes any angular frequency subscript in Eq. (92). The frequency of scattered light which satisfies phase matching is given by the roots of Eq. (92), which can be found by plotting M_Y vs Ω_1. This is illustrated for SRS and SWS in Fig. 3, and for SBS in Fig. 4, for the parameters given in Table I and $n_e/n_{crit} = 0.15$.

The dispersion relations given in Eq. (92) are plotted as a function of ω_1/ω_0 and n_e/n_{crit} for scattering geometries $(c_1, c_2) = (-1, 1), (1, 1), (1, -1)$, in Figs. 5–7, respectively. The two

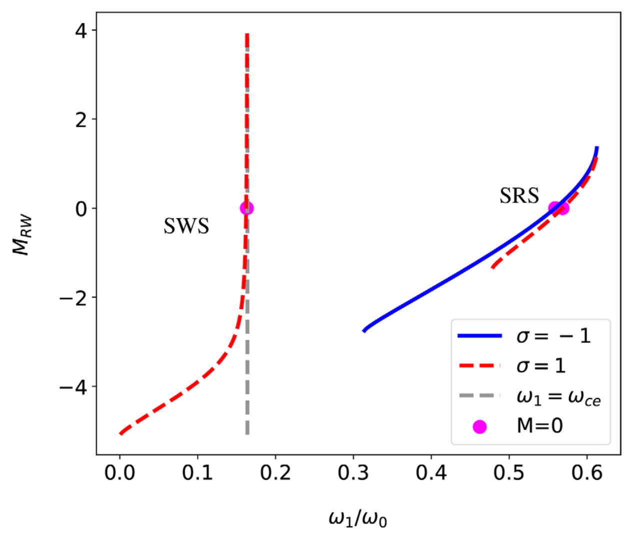

FIG. 3. The dispersion relation for SRS and SWS, M_{RW} is plotted vs ω_1/ω_0. Its roots $M_{RW} = 0$ are indicted by magenta points. This is for backscatter ($c_1 = -1, c_2 = 1$) and the parameters of Table I plus $n_e/n_{crit} = 0.15$. SWS is possible for a right-polarized pump (red) but cannot occur when the pump is left polarized (blue).

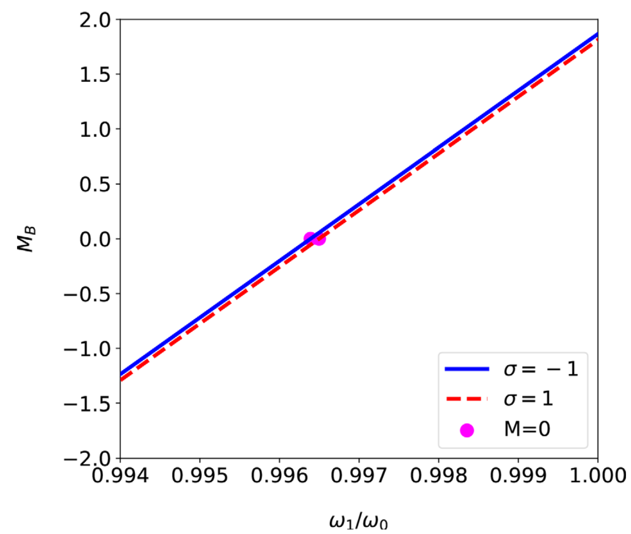

FIG. 4. The dispersion relation for SBS, M_B is plotted vs ω_1/ω_0, for the same parameters as Fig. 3. Its roots $M_B = 0$ are indicted by magenta points. The roots of M_B occur at similar, but not identical ω_1/ω_0 for a left- and right-polarized pump.

dispersion relations, M_{RW} and M_B, have been overplotted. To distinguish between them, M_{RW} has been cross-hatched, while M_B has not. The color scale for M applies to both M_{RW} and M_B. The regions of Figs. 5–7 where M is not real are colored gray. The regions of the plot

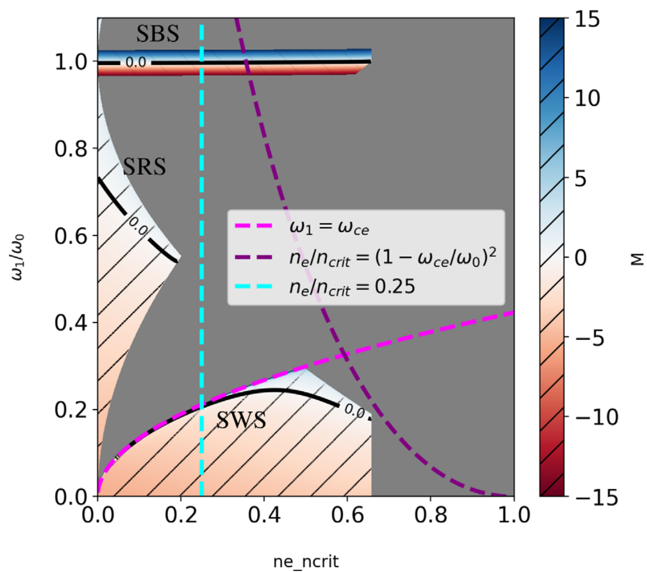

FIG. 5. The dispersion relations for SWS and SRS (M_{RW}) and SBS (M_B) vs electron density and scattered light frequency. $T_e = 4$ keV, $T_i = 2$ keV, $\omega_{ce}/\omega_{pe} = 0.423$, and we consider backscatter ($c_1 = -1, c_2 = 1$). M_{RW} is distinguished by cross-hatching. The roots of M are plotted as black contours which have been labeled appropriately. Three other curves have been plotted: $n_e/n_{crit} = 0.25$, the maximum density at which SRS occurs, $\omega_1 = \omega_{ce}$, the maximum SWS frequency, and $n_e/n_{crit} \geq (1-\omega_{ce}/\omega_0)^2$, the *minimum* density at which SWS can occur in a cold plasma. Note that M_{RW} adheres to only the first two of these approximate analytic limits.

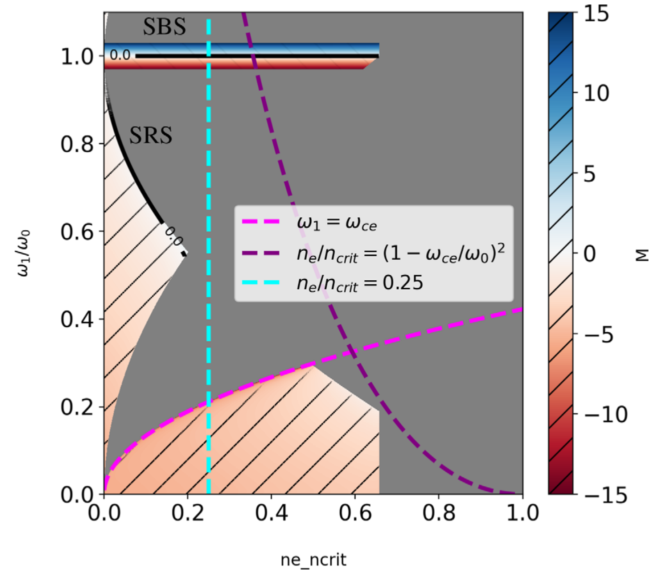

FIG. 6. As Fig. 5, but for forward scatter ($c_1 = c_2 = 1$). Only SRS can occur for this geometry. While SBS is kinematically possible, the ion wave has $k_2, \omega_2 = 0$, and SBS has 0 growth rate. Thus, the solution plotted is spurious. For this geometry, SWS is kinematically disallowed.

where $M_{RW,B} \neq 0$ serve only to illustrate the root-finding method employed: to ensure we have correctly identified roots, we check that $M_{RW,B}$ has changed the sign. The roots of M have been computed numerically and are plotted as black contours. These contours indicate whether SRS, SBS, or SWS can occur for the geometry and plasma conditions considered and illustrate the relationship between the

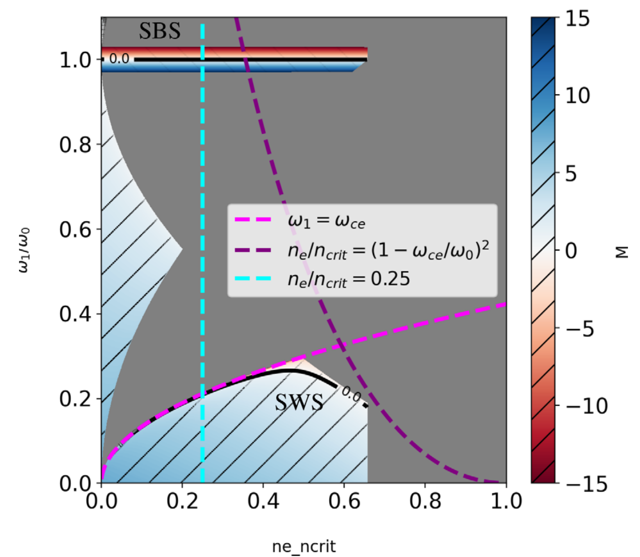

FIG. 7. As Fig. 5, but for $c_1 = 1$ and $c_2 = -1$. For this geometry, phase matching is only satisfied for SWS, and unphysical SBS as in Fig. 6. As in Fig. 5, $M_{RW} = 0$ is only satisfied for densities above the minimum normalized electron density in a cold plasma, $n_e/n_{crit} \geq (1-\omega_{ce}/\omega_0)^2$, which is plotted in purple.

normalized plasma density and scattered EMW frequency for each of these processes. The contours which correspond to a given parametric process are appropriately labeled.

In Figs. 5 and 6, a sharp decrease can be seen in the frequency of SRS scattered light with increasing plasma density. Also in Figs. 5 and 7, the frequency of SWS scattered light rises with electron density before reaching a maximum, and falling. It is often useful to obtain limits in parameter space beyond which phase matching cannot occur. For example, in an unmagnetized plasma, SRS is only possible for $n_e/n_{crit} < 0.25$. The region of parameter space in which SWS can occur is also restricted, as $\omega_1 \le \omega_{ce}$. Using the same method as for SRS, the following inequality is obtained for the normalized electron densities at which SWS can occur in a cold plasma

$$\frac{n_e}{n_{crit}} \ge (1 - \omega_{ce}/\omega_0)^2. \tag{93}$$

These three limits are shown in Figs. 5–7 in cyan, magenta, and purple, respectively. Note that the contours for SRS and SWS always lie within $n_e/n_{crit} < 0.25$ and $\omega_1 \le \omega_{ce}$, respectively, as expected. SWS does *not* respect Eq. (93), as discussed further below.

A. Stimulated Raman scattering: SRS

The dispersion relation for SRS is given by Eq. (92), where $c_2 = 1$. For a cold plasma with $V_e = 0$, we find $\Omega_2 = \Omega_p$ always, so $\Omega_1 = 1 - \Omega_p$. This is true with or without a background field B_{eq}. Thus, any effect of B_{eq} on Ω_1 is "doubly small," in that it also relies on thermal effects. For no background field $\Omega_{ce} = 0$, we obtain the usual solutions, which for $V_e \ll 1$ and $\Omega_p \ll 1$ are $\Omega_1 \approx 1 - \Omega_p - (\Omega_p/2) V_e^2$ for $c_1 = 1$ (forward scatter), and $\Omega_1 \approx 1 - \Omega_p - (2/\Omega_p)V_e^2$ for $c_1 = -1$ (backscatter).

Including a weak background field, we write $\Omega_1 \approx \Omega_{1U} + \delta\Omega_1$ where Ω_{1U} is the solution for $\Omega_{ce} = 0$: $M[\Omega_{1U}, \Omega_{ce} = 0] = 0$. We have $M[\Omega_{1U} + \delta\Omega_1, \Omega_{ce}] \approx M[\Omega_{1U}, 0] + \delta\Omega_1(\partial M/\partial\Omega_1) + \Omega_{ce}\partial M/\partial\Omega_{ce} = 0$, which gives $\delta\Omega_1 \approx \alpha\Omega_{ce}$ with $\alpha = -(\partial M/\partial\Omega_{ce})/(\partial M/\partial\Omega_1)$. All partials are evaluated at $\Omega_1 = \Omega_{1U}$ and $\Omega_{ce} = 0$. One can find a formula for α, but it is unilluminating. We quote the result in the limit that $V_e \ll 1$ and $\Omega_p \ll 1$

$$\alpha \approx c_1 \left(2/\Omega_p^2 + 1/\Omega_p + 2\right)^{\frac{1-c_1}{2}} \sigma_0 V_e^2 \Omega_p^3. \tag{94}$$

The full numerical solution of M_{RW} [see Eq. (92)] is plotted in Figs. 8 and 9 for the plasma conditions given in Table I and the first row of Table III. The frequencies, wave vectors, and, if applicable, the polarizations of the e/m and e/s waves at which phase-matching conditions are met are illustrated by parallelograms. Specifically, Figs. 8 and 9 correspond to forward and back-SRS, respectively.

The shift in wavelength of SRS light due to the presence of the external magnetic field, $\Delta\lambda_1 = \lambda_1 - \lambda_1(\omega_{ce} = 0)$, is given by

$$\frac{\Delta\lambda_1}{\lambda_0} = \omega_0 \left(\frac{1}{\omega_1} - \frac{1}{\omega_1(\omega_{ce} = 0)}\right). \tag{95}$$

Substituting from Eq. (85), and treating temperature and magnetic field as small perturbations in Ω_1 as detailed above, we derive the following expression for $\Delta\lambda_1$ to first order in Ω_{ce} and Ω_{pe}^2

$$\frac{\Delta\lambda_1}{\lambda_0} \approx -\frac{\delta\Omega_1}{\Omega_{1U}^2} \tag{96}$$

or, equivalently,

$$\Delta\lambda_1(\mathrm{nm}) \approx -c_1\lambda_0^2(\mu\mathrm{m}^2)\frac{5.48 \times 10^{-4}}{\Omega_{1U}^2} Te(\mathrm{keV})\left(\frac{n_e}{n_{crit}}\right)^{3/2} \times B(T)\left(2\frac{n_{crit}}{n_e} + \sqrt{\frac{n_{crit}}{n_e}} + 2\right)^{\frac{1-c_1}{2}} \sigma_0 \tag{97}$$

in practical units. Under the conditions given in Table I, for $n_e/n_{crit} = 0.15$ and $B = 100$ T for SRS backscattered light from a left-polarized pump wave, the analytic approximation yields $\Delta\lambda_1 = -0.041$ nm,

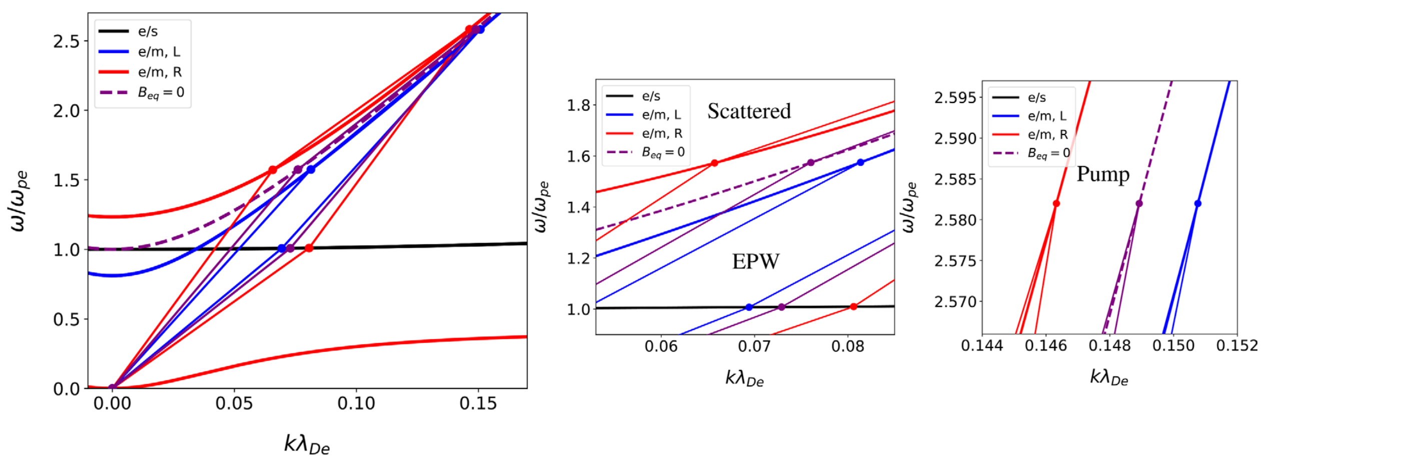

FIG. 8. Phase-matching parallelograms for forward-SRS light for plasma conditions given in Table I, with $n_e/n_{crit} = 0.15$. The right- and left-polarized e/m waves are plotted in red and blue, respectively, while the unmagnetized e/m wave and the electrostatic EPW are shown in purple and black, respectively. The phase-matching parallelograms are color-coded according to the polarization of the pump wave. The pump frequency ω_0 is fixed in all cases, which gives slightly different k_0s from the relevant dispersion relations. The scattered e/m frequencies ω_1 are *nearly* but not exactly the same, though this is very hard to see visually. The pump and scattered e/m waves have the same handedness.

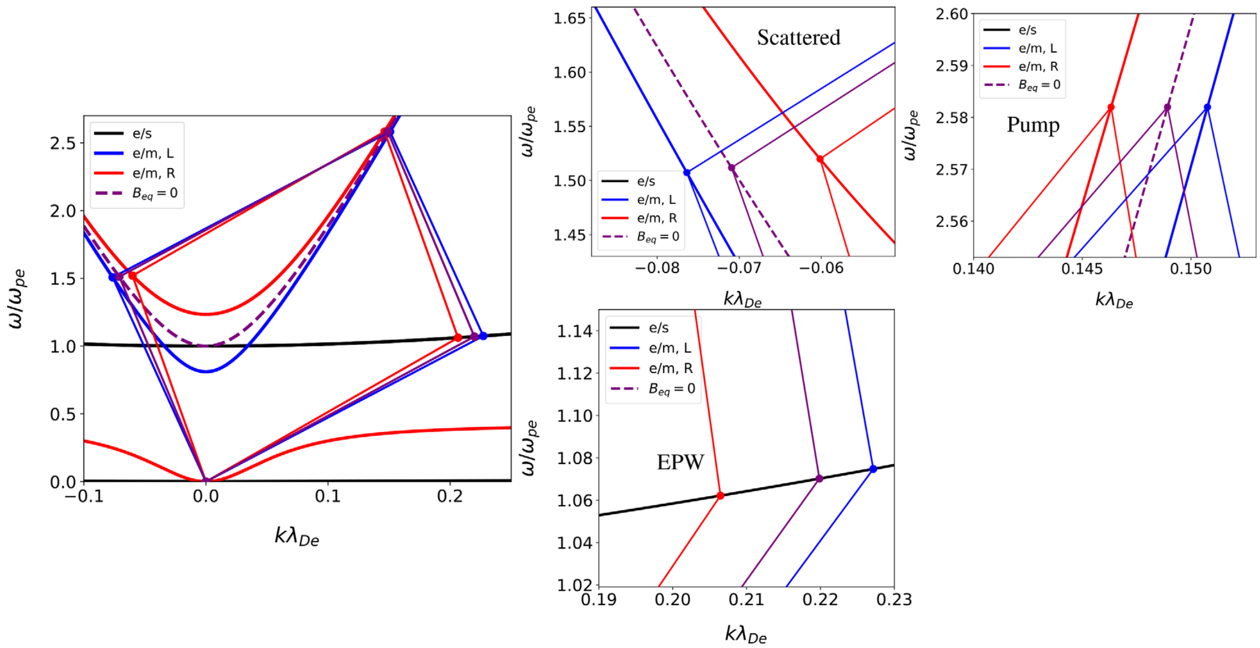

FIG. 9. Phase-matching parallelograms for backward-SRS light: otherwise same as Fig. 8.

compared to the full numerical solution, which gives $\Delta\lambda_1 = -0.046$ nm. Typically, in NIF-type experiments, the wavelength of back-SRS light is in the range of 500–600 nm, with a spectral width of 5–10 nm due to damping and gradients. Given that this is the case, detecting sub-Angstrom shifts in this spectrum presents a significant challenge. This first-order approximation of $\Delta\lambda_1$ agrees reasonably closely with the full numerical computation of $\Delta\lambda_1$, which is plotted as a function of ω_{ce}/ω_{pe} for $T_e = 2$ keV, 4 keV, and $n_e/n_{crit} = 0.05, 0.15$ in Figs. 10(a) and 10(b), for forward and back-SRS light, respectively. Similarly, the first order approximation and full numerical solution for $\Delta\lambda_1$ is shown as a function of T_e for forward and back SRS in Figs. 11(a) and 11(b), respectively, for $n_e/n_{crit} = 0.05$ and $\omega_{ce}/\omega_{pe} = 0.1$. The effect of electron density and temperature becomes particularly significant for forward and backward-SRS light from a right-polarized pump as $\omega_{ce} \to \omega_{pe}$, as in this limit, $\Delta\lambda_1 \to \infty, -\infty$, respectively.

B. Stimulated Brillouin scattering: SBS

The phase-matching relation for SBS, $M_B = 0$ is derived in Sec. IV, and given in Eq. (92). A phase-matching diagram is shown in Fig. 12 for the same conditions as Fig. 8. Exact forward SBS ($c_1 = 1$) is not considered since in our strictly 1D geometry it does not occur. $M_B = 0$ has a spurious root for $k_2 = \omega_2 = 0$, which connects to near-forward scatter for small but nonzero angle between $\vec{k}_0$ and $\vec{k}_1$. The SBS growth rate is zero for $k_2 = 0$, so we discuss only backscatter ($c_1 = -1$, $c_2 = 1$). For $\Omega_{ce} = 0$, the exact solution is

$$\Omega_{1U} = \frac{1 - 2\eta_0 V_s + V_s^2}{1 - V_s^2} \approx 1 - 2\eta_0 V_s \tag{98}$$

with $\eta_0 \equiv (1 - \Omega_{pe}^2)^{1/2}$. The approximate form for $V_s \ll 1$ is typically quite accurate. The correction for a weak B field and to leading order in V_s^2 is

$$\delta\Omega_1 = \sigma_0 \Omega_{pe}^2 V_s \Omega_{ce}(1 + V_s). \tag{99}$$

For simplicity, we set the final factor to 1 below. As with SRS, the correction is doubly small since it scales with the product of $V_s \propto T_e^{1/2}$ and Ω_{ce}. The scattered wavelength shift $\delta\lambda_1 \equiv \lambda_1 - \lambda_1[\Omega_{ce} = 0]$, evaluated at $\Omega_{1U} = 1$, is

$$\frac{\delta\lambda_1}{\lambda_0} \approx -\sigma_0 \Omega_{pe}^2 V_s \Omega_{ce}(1 + V_s). \tag{100}$$

In practical units,

$$\delta\lambda_1(\text{Ang.}) \approx -9.67 \times 10^{-4} \sigma_0 \frac{n_e}{n_{crit}} B(T) \times \sqrt{\frac{Z_i T_e(\text{keV})}{A_i}\left(1 + \frac{3T_i(\text{keV})}{Z_i T_e(\text{keV})}\right)} \lambda_0^2(\mu\text{m}^2). \tag{101}$$

This is an extremely small value for ICF conditions. For the parameters shown in Table III, with $\lambda_0 = 351$ nm, $n_e/n_{crit} = 0.15$, $B = 100$T,

TABLE III. Electron densities and magnetic field strengths which correspond to the normalized parameters considered throughout this paper, for typical NIF and CO_2 laser wavelengths. $\frac{\omega_{ce}}{\omega_{pe}} = 0.423$ in all cases.

Laser wavelength (μm)	n_e/n_{crit}	n_e (cm^{-3})	B_{eq} (T)
0.351 (NIF)	0.15	1.36×10^{21}	5000
0.351	0.01	9.05×10^{19}	1290
10.6 (CO_2)	0.15	1.49×10^{18}	166
10.6	0.01	9.92×10^{16}	42.7

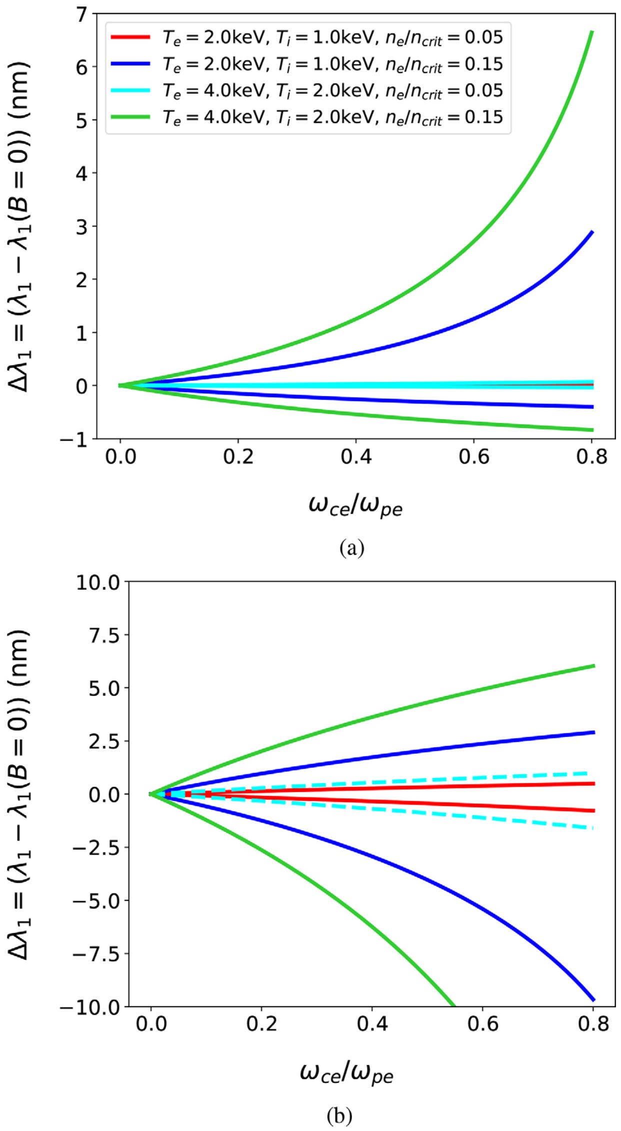

FIG. 10. $\Delta\lambda_1$, the difference in wavelength of forward [10(a)] and backward [10(b)] SRS light in a magnetized vs an unmagnetized plasma, for $T_e = 2.0$ keV, 4.0 keV, $n_e/n_{crit} = 0.05$, 0.15 and $\lambda_0 = 351$ nm. For [forward, backward] SRS, $\Delta\lambda_1$ is $[> 0, < 0]$ for a right-polarized pump and $[< 0, > 0]$ for a left-polarized pump.

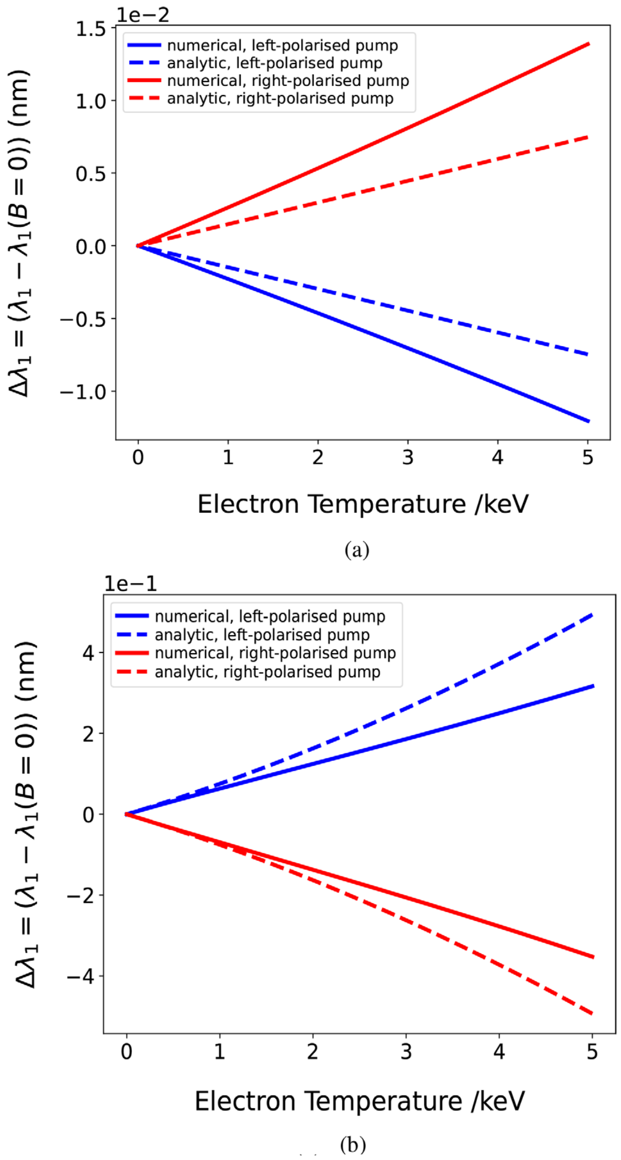

FIG. 11. $\Delta\lambda_1$ of forward [11(a)] and backward [11(b)] SRS light, plotted for $\omega_{ce}/\omega_{pe} = 0.1$, $\frac{n_e}{n_{crit}} = 0.05$, and $\lambda_0 = 351$ nm. Full numerical solutions are unbroken lines, first-order analytic approximations are dashed lines.

and a right-polarized pump, the analytic approximation gives $\delta\lambda_1 \approx -2.37$ pm, whereas the full numerical solution gives $\delta\lambda_1 \approx -2.41$ pm. The variation of $\Delta\lambda_1$ with $\omega_{ce}/\omega_{crit}$ and T_e is shown in Figs. 13 and 14, respectively.

C. Stimulated whistler scattering: SWS

We now discuss SWS, which only occurs with a background magnetic field. It resembles SRS, except the scattered e/m wave is a low-frequency whistler ($\omega_1 < \omega_{ce}$). For a cold plasma, this imposes a *minimum* density of $n_e/n_{crit} \geq (1 - \omega_{ce}/\omega_0)^2$ to satisfy frequency matching, as opposed to a *maximum* of $n_e/n_{crit} < 1/4$ for SRS. Forward ($c_1 = +1, c_2 = -1$) and backward ($c_1 = -1, c_2 = +1$) SWS are both kinematically allowed though forward SWS can only occur for a plasma wave propagating counter to the pump: $c_2 = -1$. The phase-matching condition M_{RW} for SWS, given in Eq. (92), is identical to that of SRS except that $c_2 = \pm 1$. Figures 15 and 16 show SWS phase-matching diagrams for the allowed geometries and for a range of n_e/n_{crit}, ω_{ce}/ω_{pe} and T_e.

The relationship between ω_1/ω_0, $k_2\lambda_{De}$ and ω_{ce}/ω_{pe} is shown in Figs. 17 and 18 for $(c_1, c_2) = (-1, 1), (1, -1)$, respectively, for a range of plasma densities and temperatures. The frequency of the scattered

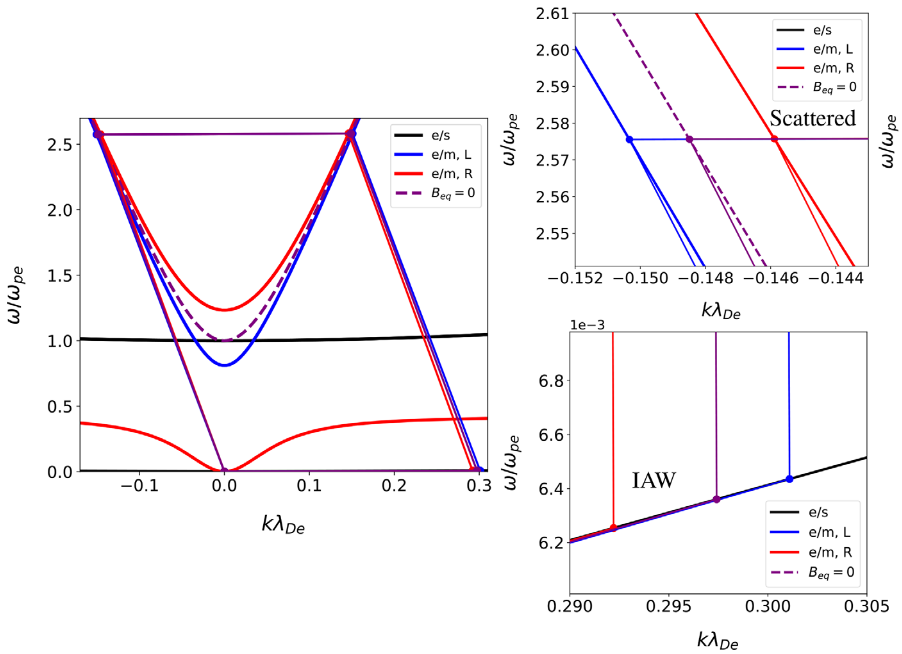

FIG. 12. Phase-matching parallelograms for backward-SBS, otherwise same as Fig. 8. Electrostatic IAW shown in black.

EMW increases with increasing magnetic field strength, before saturating. The rate of increase with ω_{ce}/ω_{pe} and the values of ω_1/ω_0 and ω_{ce}/ω_{pe} at which saturation occurs vary with plasma density and temperature. Increasing T_e decreases the ω_1/ω_0 at which the trend saturates, while increasing n_e/n_{crit} causes the observed trend to saturate at lower ω_1/ω_0 and ω_{ce}/ω_{pe}. $k_2\lambda_{De}$ is plotted to indicate the magnitude of Landau damping, which is expected to significantly reduce SWS growth for $k_2\lambda_{De} \gtrsim 0.5$. In the opposite limit, the SWS growth rate approaches zero as $k_2\lambda_{De} \to 0$.

The wavelength of SWS scattered light is

$$\lambda_1(\mu\text{m}) = \frac{\omega_{ce}}{\omega_1}\frac{10\,709.7}{B(T)}. \tag{102}$$

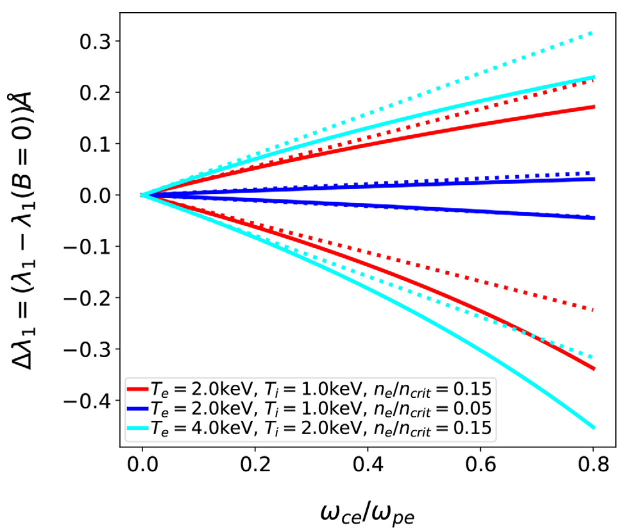

FIG. 13. $\delta\lambda_1$, the difference in wavelength of backward-SBS light in a magnetized vs an unmagnetized plasma, for three combinations of electron temperatures and densities $T_e = 2.0$ keV, 4.0 keV, and $n_e/n_{crit} = 0.05$, 0.15, where the ratio of electron and ion temperature is kept constant: $T_e/T_i = 2$. The laser wavelength, $\lambda_0 = 351$ nm. The full numerical solutions and their analytic counterparts are plotted as unbroken and dashed lines, respectively. $\Delta\lambda_1[<0, >0]$ for a right- or left-polarized pump, respectively.

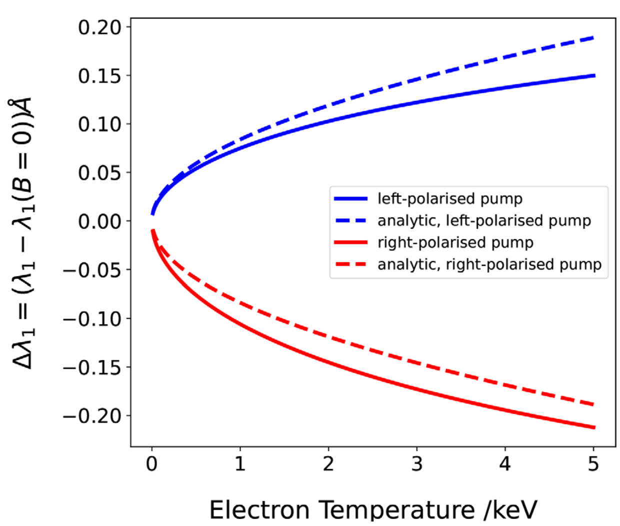

FIG. 14. $\Delta\lambda_1$ of backwards SBS light, plotted for $\omega_{ce}/\omega_{pe} = 0.423$, $\frac{n_e}{n_{crit}} = 0.15$ and $\lambda_0 = 351$ nm. Full numerical solutions are unbroken lines, analytic approximations as dashed lines.

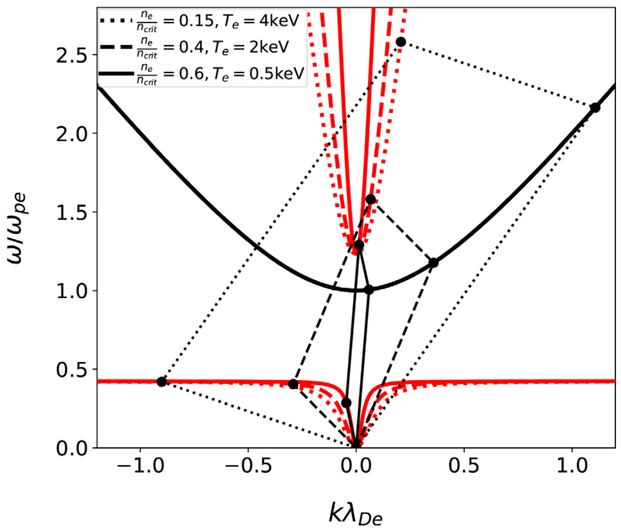

FIG. 15. Phase-matching parallelogram for forward SWS: $c_1 = 1, c_2 = -1$, where $\omega_{ce}/\omega_{pe} = 0.423$ and $T_i = T_e/2$.

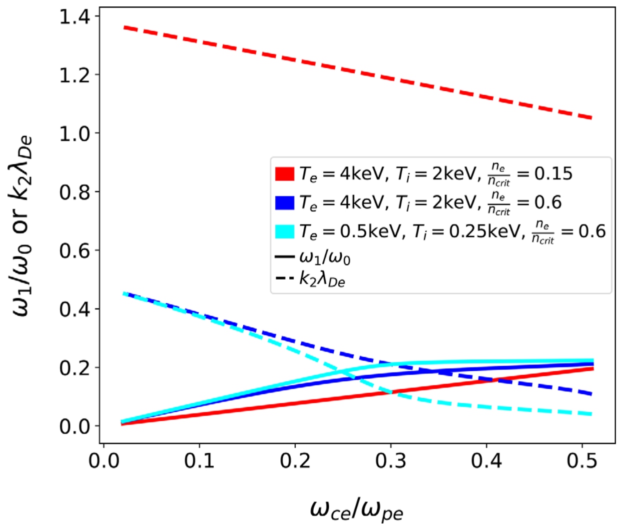

FIG. 17. Phase-matching parallelogram for backward SWS ($c_1 = -1, c_2 = 1$), for a range of electron densities and temperatures, where $\omega_{ce}/\omega_{pe} = 0.423$ and $T_i = T_e/2$.

For the bottom rows of Table IV, $n_e/n_{crit} = 0.15$, $\omega_{ce}/\omega_{pe} = 0.423$, and $\omega_1 \approx \omega_{ce}$. For a pump wavelength of $0.351\,\mu$m, we have $B = 5000$ T and $\lambda_1 \approx 2.14\,\mu$m. This is in the near infrared, where detectors exist but are not commonly fielded on ICF lasers. More realistic B fields will be much lower, and λ_1 much longer.

In order for SWS scattered light to be detected, it must first leave the plasma and propagate to a detector. Given the long wavelength of SWS scattered light, there is a possibility that changing plasma conditions experienced by the wave as it propagates through the plasma may cause it to become evanescent. Consider Eq. (77). Rearranging for k, we obtain

$$c^2k^2 = \omega^2 - \frac{\omega_{pe}^2}{1 - \sigma\dfrac{\omega_{ce}}{\omega}}. \tag{103}$$

We see that for $\omega^2 > \frac{\omega_{pe}^2}{1-\sigma\frac{\omega_{ce}}{\omega}}$, k is real and the wave can propagate. If the reverse is true, k is imaginary and the wave is evanescent. ω_{pe} and ω_{ce} vary in space and generally go to zero far from the target. If B tends to zero too rapidly, the dispersion relation tends to the unmagnetized one, $c^2k^2 = \omega^2 - \omega_{pe}^2$. In this case, if n_e exceeds the critical density of

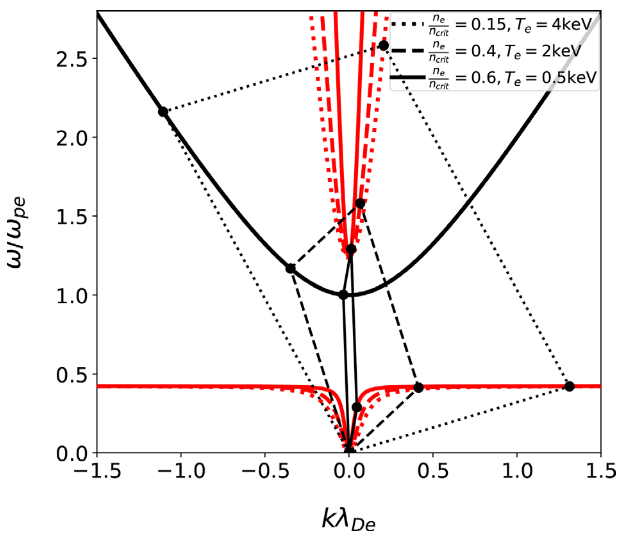

FIG. 16. Frequency (unbroken lines) of forward-SWS scattered light ($c_1 = 1$, $c_2 = -1$), and Langmuir wave $k_2\lambda_{De}$ (dashed lines) for various plasma densities, $n_e/n_{crit} = 0.6, 0.15$, and species temperatures, $T_e = 4, 0.5$ keV, $T_i = T_e/2$ keV. $k_2\lambda_{De}$ is plotted to indicate the strength of Landau damping.

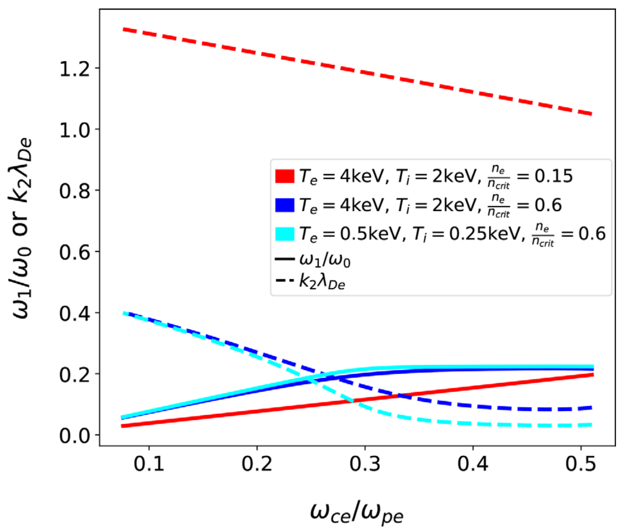

FIG. 18. Frequency backward SWS light with $c_2 = 1$, for $n_e/n_{crit} = 0.6, 0.15$ and $T_e = 4, 0.5$ keV.

TABLE IV. Frequencies of stimulated whistler scattered light for several n_e/n_{crit} and T_e (ion temperature, $T_i = T_e/2$), and their corresponding values of the normalized EPW wavenumber. For all cases, $\omega_{ce}/\omega_{pe} = 0.423$. The rightmost column is the minimum n_e/n_{crit} for SWS to occur in a cold plasma.

c_1	c_2	n_e/n_{crit}	T_e (keV)	ω_1/ω_0	ω_1/ω_{ce}	$k_2\lambda_{De}$	$(1-\frac{\omega_{ce}}{\omega_0})^2$
−1	1	0.6	0.5	0.2212	0.6752	0.0592	0.452
1	−1	0.6	0.5	0.224	0.6836	0.0336	0.452
−1	1	0.6	4	0.1995	0.609	0.1502	0.452
1	−1	0.6	4	0.2163	0.6601	0.0883	0.452
−1	1	0.4	2	0.2557	0.9557	0.3582	0.5365
1	−1	0.4	2	0.2615	0.9776	0.3479	0.5365
−1	1	0.15	4	0.1623	0.9904	1.1074	0.6992
1	−1	0.15	4	0.1631	0.9955	1.106	0.6992

the SWS scattered light wave, the wave will be reflected and will not reach the detector. However, if the magnetic field strength decreases slowly enough and/or the electron density decreases quickly enough, the wave will escape the plasma. Then, $\omega_{pe} = 0$ and $ck = \omega$, that is, it becomes a vacuum light wave and can propagate to the detector.

We now discuss the variation of SWS with plasma parameters. For finite T_e, Langmuir-wave frequency increases, an effect comparable to an increase in electron density. This enables SWS to occur at densities lower than the minimum density in a cold plasma, given in Eq. (93). We see this in Fig. 16, where the lowest density shown, $n_e/n_{crit} = 0.15$, corresponds to the highest pump frequency and a very high Langmuir-wave frequency, $\omega_2/\omega_{pe} > 2$. This requires a large $k_2\lambda_{De} > 1$, which entails considerable Landau damping and, therefore, a low SWS growth rate. Although growth rates are beyond the scope of this paper, other work establishes that they generally are $\propto k_2^p$ (for some power p) when $k_2\lambda_{De}$ is small and decrease with increasing Landau damping for large $k_2\lambda_{De}$. This means there is an effective low-density cut-off, below which SWS is kinematically allowed but strongly damped. In the opposite limit, as n_e approaches n_{crit} (such as $n_e/n_{crit} = 0.6$ in Figs. 16 and 17 and Table IV), k_2 becomes small, and Landau damping is negligible; however, the growth rate of SWS also tends to 0. There is, thus, an intermediate range of n_e in which the growth rate is optimal, and $k_2\lambda_{De}$ is moderate. The case where $n_e/n_{crit} = 0.4$ and $T_e = 2\,\text{keV}$ shown in Figs. 16 and 15 and Table IV typifies this regime.

V. CONCLUSION

We presented a warm-fluid theory for magnetized LPI, for the simple geometry of all wavevectors parallel to a uniform, background field. The field affects the electromagnetic linear waves in a plasma though the electrostatic waves are unaffected for our geometry. Specifically, the right and left circular polarized e/m waves become non-degenerate and form the natural basis, as opposed to linearly polarized waves. This allows for Faraday rotation, which could be significant on existing ICF laser facilities for magnetic fields imposable with current technology. The field introduces two new e/m waves, the ion cyclotron and whistler wave, which have no analogues in an unmagnetized plasma.

We found a parametric dispersion relation to first order in the parametric coupling, Eq. (67), analogous to the classic 1974 work of Drake *et al.*[28] We then focused on the kinematics of phase matching for three-wave interactions. Since the right and left circular polarized light waves have different k vectors for the same frequency, the background field introduces a small shift in the scattered SRS and SBS frequencies compared to the unmagnetized case. The sign of the shift depends on the pump polarization and forward vs backward scatter. The shift's magnitude increases with magnetic field, electron temperature, and plasma density. The wavelength shifts are $\lesssim 1$ Ang. for SRS, and $\lesssim 0.1$ Ang. for SBS, for plasma and magnetic field conditions currently accessible on lasers like NIF. Such small shifts would be extremely challenging to detect.

The new waves supported by the background B field also allow for new parametric processes, such as SWS, which we studied in detail. In this process, a light wave decays to a whistler wave and Langmuir wave. This is analogous to Raman scattering, with the whistler replacing the scattered light wave. We expect SWS scattered light to be infrared, with wavelength 1–100 μm for fields of 10 kT–100 T. The whistler wavelength was found to decrease with increasing magnetic field strength and increase with increasing plasma density and temperature. In a cold plasma ($T_e = 0$), there is a *minimum* density for SWS to satisfy phase matching, namely, $n_e/n_{crit} > (1-\omega_{ce}/\omega_0)^2$. Finite T_e allows us to circumvent this limit, at the price of high Langmuir-wave $k\lambda_{De}$, and thus, strong Landau damping. We expect an analysis of SWS growth rates, including Landau damping, to show maximum growth for moderate $k\lambda_{De}$.

Much work remains to be done on magnetized LPI. This paper does not discuss parametric growth rates though they are contained in our parametric dispersion relation (without damping or kinetics), and others have studied them in the limit of weak coupling.[22] It is important to know when the two circularly polarized light waves generated by a single linearly polarized laser (incident from vacuum) should be treated as independent pumps, with half the intensity of (and, thus, lower growth rates than) the original laser. This likely occurs when the wavevector spread exceeds an effective bandwidth set by damping, inhomogeneity, or parametric coupling.

Two major limitations to our model are the restriction to wavevectors parallel to the background field, and the lack of kinetic effects especially in the plasma waves. Propagation at an angle to the B field opens up many rich possibilities, including waves of mixed e/m and e/s character, and B field effects on the e/s waves. In the case of perpendicular propagation, the e/s waves become Bernstein waves. Adding kinetics is essential to understanding parametric growth in many systems of practical interest, where collisionless (Landau) damping is dominant. This also raises the so-called Bernstein-Landau paradox, since Bernstein waves are naïvely undamped for any field strength.

If these issues can be resolved, we envisage magnetized LPI modeling tools analogous to existing ones for unmagnetized LPI. This was one of the main initial motivations for this work. For instance, linear kinetic coupling in the convective steady state and strong damping limit has been a workhorse in ICF for many years, such as for Raman and Brillouin backscatter[36] and crossed-beam energy transfer.[35] A magnetized generalization of this needs to handle propagation at arbitrary angles to the B field as well as arbitrary field strength. Among other things, it must correctly recover the unmagnetized limit. A suitable linear, kinetic, magnetized dielectric function will be one of the key enablers.

The dispersion relation presented in this work does not account for plasma inhomogeneities, which are highly significant for NIF and

MAGLIF campaigns. To include these effects, an approach similar to the one utilized for DEPLETE[36] could be employed. This treatment assumes that the length scale of the inhomogeneity is greater than the wavelength of the pump and scattered waves, which allows the scattered and plasma waves to be treated as collections of monoenergetic carrier waves with slowly varying amplitudes in time and space. Frequency-matching conditions, and, hence, the gain rate for SRS and SBS, vary with the plasma density, as do the refracted paths of the scattered light, which are computed using ray-tracing. The spectrum of scattered light is obtained by integrating the spatially varying gain rate over the inhomogeneous density profile along the paths of the refracted rays.

ACKNOWLEDGMENTS

It is a pleasure to thank Y. Shi and B. I. Cohen for many fruitful discussions. This work was performed under the auspices of the U.S. Department of Energy by Lawrence Livermore National Laboratory under Contract No. DE-AC52–07NA27344. This document was prepared as an account of work sponsored by an agency of the United States government. Neither the United States government nor Lawrence Livermore National Security, LLC, nor any of their employees makes any warranty, expressed or implied, or assumes any legal liability or responsibility for the accuracy, completeness, or usefulness of any information, apparatus, product, or process disclosed, or represents that its use would not infringe privately owned rights. Reference herein to any specific commercial product, process, or service by trade name, trademark, manufacturer, or otherwise does not necessarily constitute or imply its endorsement, recommendation, or favoring by the United States government or Lawrence Livermore National Security, LLC. The views and opinions of authors expressed herein do not necessarily state or reflect those of the United States government or Lawrence Livermore National Security, LLC, and shall not be used for advertising or product endorsement purposes.

AUTHOR DECLARATIONS

Conflict of Interest

The authors have no conflicts to disclose.

DATA AVAILABILITY

Data sharing is not applicable to this article as no new data were created or analyzed in this study.

REFERENCES

[1]G. E. Kemp, J. D. Colvin, B. E. Blue, and K. B. Fournier, "Simulation study of enhancing laser driven multi-kev line-radiation through application of external magnetic fields," Phys. Plasmas **23**, 101204 (2016).

[2]D. B. Schaeffer, W. Fox, D. Haberberger, G. Fiksel, A. Bhattacharjee, D. H. Barnak, S. X. Hu, and K. Germaschewski, "Generation and evolution of high-mach-number laser-driven magnetized collisionless shocks in the laboratory," Phys. Rev. Lett. **119**, 025001 (2017).

[3]S. A. Slutz, M. C. Herrmann, R. A. Vesey, A. B. Sefkow, D. B. Sinars, D. C. Rovang, K. J. Peterson, and M. E. Cuneo, "Pulsed-power-driven cylindrical liner implosions of laser preheated fuel magnetized with an axial field," Phys. Plasmas **17**, 056303 (2010).

[4]M. R. Gomez, S. A. Slutz, A. B. Sefkow, D. B. Sinars, K. D. Hahn, S. B. Hansen, E. C. Harding, P. F. Knapp, P. F. Schmit, C. A. Jennings, T. J. Awe, M. Geissel, D. C. Rovang, G. A. Chandler, G. W. Cooper, M. E. Cuneo, A. J. Harvey-Thompson, M. C. Herrmann, M. H. Hess, O. Johns, D. C. Lamppa, M. R. Martin, R. D. McBride, K. J. Peterson, J. L. Porter, G. K. Robertson, G. A. Rochau, C. L. Ruiz, M. E. Savage, I. C. Smith, W. A. Stygar, and R. A. Vesey, "Experimental demonstration of fusion-relevant conditions in magnetized liner inertial fusion," Phys. Rev. Lett. **113**, 155003 (2014).

[5]R. Jones and W. Mead, "The physics of burn in magnetized deuterium-tritium plasmas: Spherical geometry," Nucl. Fusion **26**, 127–137 (1986).

[6]I. Lindemuth and R. Kirkpatrick, "Parameter space for magnetized fuel targets in inertial confinement fusion," Nucl. Fusion **23**, 263–284 (1983).

[7]M. R. Edwards, Y. Shi, J. M. Mikhailova, and N. J. Fisch, "Laser amplification in strongly magnetized plasma," Phys. Rev. Lett. **123**, 025001 (2019).

[8]W. L. Kruer, *The Physics of Laser Plasma Interactions* (Westview Press, Boulder, CO, 2003).

[9]J. D. Lindl, P. Amendt, R. L. Berger, S. G. Glendinning, S. H. Glenzer, S. W. Haan, R. L. Kauffman, O. L. Landen, and L. J. Suter, "The physics basis for ignition using indirect-drive targets on the national ignition facility," Phys. Plasmas **11**, 339–491 (2004).

[10]G. Velarde, Y. Ronen, and J. M. Martinez-Val, *Nuclear Fusion by Inertial Confinement: A Comprehensive Treatise* (CRC Press, 1993), pp. 360–361.

[11]R. K. Kirkwood, D. J. Strozzi, P. A. Michel, D. A. Callahan, B. Raymond, G. Gururangan, B. J. MacGowan, and NIF Team, "Laser backscatter damage risk assessments of NIF target experiments," in *APS Division of Plasma Physics Meeting Abstracts*, APS Meeting Abstracts, Vol. 2014 (SAO/NASA Astrophysics Data System, 2014), p. NP8-117.

[12]T. Chapman, P. Michel, J.-M. Di Nicola, R. L. Berger, P. K. Whitman, J. D. Moody, K. R. Manes, M. L. Spaeth, M. A. Belyaev, C. A. Thomas, and B. J. MacGowan, "Investigation and modeling of optics damage in high-power laser systems caused by light backscattered in plasma at the target," J. Appl. Phys. **125**, 033101 (2019).

[13]J. D. Lindl, *Inertial Confinement Fusion: The Quest for Ignition and Energy Gain Using Indirect Drive* (Springer-Verlag, 1998), Chap. 11.

[14]L. Lancia, A. Giribono, L. Vassura, M. Chiaramello, C. Riconda, S. Weber, A. Castan, A. Chatelain, A. Frank, T. Gangolf, M. N. Quinn, J. Fuchs, and J.-R. Marquès, "Signatures of the self-similar regime of strongly coupled stimulated Brillouin scattering for efficient short laser pulse amplification," Phys. Rev. Lett. **116**, 075001 (2016).

[15]J. Ren, W. Cheng, S. Li, and S. Suckewer, "A new method for generating ultraintense and ultrashort laser pulses," Nat. Phys. **3**, 732 (2007).

[16]K. H. Lehmann and G. Spatschek, "Nonlinear Brillouin amplification of finite-duration seeds in the strong coupling regime," Phys. Plasmas **20**, 073112 (2013).

[17]L. J. Perkins, B. G. Logan, G. B. Zimmerman, and C. J. Werner, "Two-dimensional simulations of thermonuclear burn in ignition-scale inertial confinement fusion targets under compressed axial magnetic fields," Phys. Plasmas **20**, 072708 (2013).

[18]L. J. Perkins, D. J. Strozzi, M. A. Rhodes, B. G. Logan, D. D. Ho, and S. A. Hawkins, "The application of imposed magnetic fields to ignition and thermonuclear burn on the National Ignition Facility," Bull. Am. Phys. Soc. **59**, 15 (2014).

[19]J. Moody, B. Pollock, H. Sio, D. Strozzi, D. Ho, C. Walsh, S. Kucheyev, B. Kozioziemski, E. Carroll, J. Fry *et al.*, "Progress on the magnetized ignition experimental platform for the National Ignition Facility," Bull. Am. Phys. Soc. **66**, 13 (2021).

[20]N. M. Laham, A. S. A. Nasser, and A. M. Khateeb, "Effects of axial magnetic fields on backward Raman scattering in inhomogeneous plasmas," Phys. Scr. **57**, 253–257 (1998).

[21]L. Stenflo and G. Brodin, "On the parametric decay of a circularly polarized wave," J. Plasma Phys. **77**, 431–435 (2011).

[22]Y. Shi, "Three-wave interactions in magnetized warm-fluid plasmas: General theory with evaluable coupling coefficient," Phys. Rev. E **99**, 063212 (2019).

[23]B. J. Winjum, F. S. Tsung, and W. B. Mori, "Mitigation of stimulated raman scattering in the kinetic regime by external magnetic fields," Phys. Rev. E **98**, 043208 (2018).

[24]D. W. Forslund, J. M. Kindel, and E. L. Lindman, "Parametric excitation of electromagnetic waves," Phys. Rev. Lett. **29**, 249–252 (1972).
[25]L. Stenflo and G. Brodin, "Parametric decay of whistler waves in electron magnetohydrodynamics," Phys. Scr. **83**, 069801 (2010).
[26]A. Kumar and V. K. Tripathi, "Stimulated scattering of a whistler off an ion Bernstein wave," Phys. Scr. **84**(6), 065505 (2011).
[27]M. Porkolab and R. P. H. Chang, "Nonlinear wave effects in laboratory plasmas: A comparison between theory and experiment," Rev. Mod. Phys. **50**, 745–795 (1978).
[28]J. F. Drake, P. K. Kaw, Y. C. Lee, G. Schmid, C. S. Liu, and M. N. Rosenbluth, "Parametric instabilities of electromagnetic waves in plasmas," Phys. Fluids **17**, 778–785 (1974).
[29]W. M. Manheimer and E. Ott, "Parametric instabilities induced by the coupling of high and low frequency plasma modes," Phys. Fluids **17**, 1413–1421 (1974).
[30]B. I. Cohen, "Compact dispersion relations for parametric instabilities of electromagnetic waves in magnetized plasmas," Phys. Fluids **30**, 2676–2680 (1987).
[31]V. Stefan, N. A. Krall, and J. B. McBride, "The nonlinear eikonal relation of a weakly inhomogeneous magnetized plasma upon the action of arbitrarily polarized finite wavelength electromagnetic waves," Phys. Fluids **30**, 3703–3712 (1987).
[32]T. H. Stix, *Waves in Plasmas*, 2nd ed. (Springer-Verlag, New York, 1992), p. 10.
[33]C. J. Randall, J. R. Albritton, and J. J. Thomson, "Theory and simulation of stimulated Brillouin scatter excited by nonabsorbed light in laser fusion systems," Phys. Fluids **24**, 1474–1484 (1981).
[34]W. L. Kruer, S. C. Wilks, B. B. Afeyan, and R. K. Kirkwood, "Energy transfer between crossing laser beams," Phys. Plasmas **3**, 382–385 (1996).
[35]P. Michel, L. Divol, E. A. Williams, S. Weber, C. A. Thomas, D. A. Callahan, S. W. Haan, J. D. Salmonson, S. Dixit, D. E. Hinkel, M. J. Edwards, B. J. MacGowan, J. D. Lindl, S. H. Glenzer, and L. J. Suter, "Tuning the implosion symmetry of ICF targets via controlled crossed-beam energy transfer," Phys. Rev. Lett. **102**, 025004 (2009).
[36]D. J. Strozzi, E. A. Williams, D. E. Hinkel, D. H. Froula, R. A. London, and D. A. Callahan, "Ray-based calculations of backscatter in laser fusion targets," Phys. Plasmas **15**, 102703 (2008).